



# The unique speciation of iron in calc-alkaline obsidians

Laurence Galois, Georges Calas

## ► To cite this version:

Laurence Galois, Georges Calas. The unique speciation of iron in calc-alkaline obsidians. Chemical Geology, 2021, 559, pp.119925 -. 10.1016/j.chemgeo.2020.119925 . hal-03493054

**HAL Id: hal-03493054**

**<https://hal.science/hal-03493054>**

Submitted on 7 Nov 2022

**HAL** is a multi-disciplinary open access archive for the deposit and dissemination of scientific research documents, whether they are published or not. The documents may come from teaching and research institutions in France or abroad, or from public or private research centers.

L'archive ouverte pluridisciplinaire **HAL**, est destinée au dépôt et à la diffusion de documents scientifiques de niveau recherche, publiés ou non, émanant des établissements d'enseignement et de recherche français ou étrangers, des laboratoires publics ou privés.



Distributed under a Creative Commons Attribution - NonCommercial 4.0 International License

## The unique speciation of iron in calc-alkaline obsidians

Laurence Galois<sup>a,\*</sup>, Georges Calas<sup>a</sup>.

<sup>a</sup> *Sorbonne Université, Muséum National d'Histoire Naturelle, CNRS, Institut de Minéralogie, de Physique des Matériaux et de Cosmochimie, IMPMC, 75005 Paris, France*

*\*corresponding author : Georges Calas, Sorbonne Université, IMPMC, BC 115, 4 place Jussieu 75005 Paris, France. [georges.calas@sorbonne-universite.fr](mailto:georges.calas@sorbonne-universite.fr)*

**Keywords:**

Obsidian

Rhyolite

Glass

Magnetite

Color

UV-visible spectroscopy

EPR

Volcanic glasses

## Abstract

Obsidians found in silicic domes and rhyolitic tuffs are an ideal system to understand the formation conditions of calc-alkaline felsic magmas. They have an unusual black to brown color. The optical absorption and Electron Paramagnetic Resonance (EPR) spectroscopic data presented in this study demonstrate that Fe-speciation in obsidians is different from that observed in other geological glasses (e.g., basaltic glasses) or in synthetic Fe-bearing silicate glasses. Iron sites partly occur in mixed valence clusters, located outside the glass structure: EPR data indicate the presence of superparamagnetic Fe-rich clusters. The absence of crystal field absorption bands extending towards the visible part of the optical spectrum, explains the original color of these glasses that do not show the blue, green or yellow hues that would be expected from the presence of Fe in the glass structure. The temperature dependence of the optical absorption is consistent with the presence of magnetite-like domains that give rise to original and efficient optical absorption processes. In particular, the optical spectra show a dramatic intensification at low temperature, with an amplitude which is not observed in synthetic glasses. The smallest magnetite-like clusters are transparent enough to contribute to the original absorption bands of obsidians, intensified through exchange-coupled pairing and  $^{[6]}\text{Fe}^{2+}\text{-}^{[6]}\text{Fe}^{3+}$  and/or  $^{[6]}\text{Fe}^{2+}\text{-}^{[6]}\text{Ti}^{4+}$  Inter-Valence Charge Transfer (IVCT) processes. The largest ones will contribute to the black color of obsidians. The presence of Fe-clusters in calc-alkaline obsidians reflects the last events of the magmatic history during emplacement and cooling. This unusual Fe-speciation suggests that the Fe-redox states in obsidians cannot be considered as a quenched witness of the initial magma.

## 1. Introduction

Obsidians are aphyric volcanic rocks formed during explosive or effusive eruptions of viscous, silica-rich magmas. They occur in rare silicic domes or as clasts in rhyolitic tuff flows, by contrast to the predominant explosive character of the emplacement of most high silica magmas. In addition to their worldwide distribution, obsidians serve as an ideal system to model volcanic processes (Stevenson et al., 1995) and to understand the formation conditions of felsic magmas (Leonhardt et al., 2006; Rust and Cashman, 2007). Obsidians are also a unique cultural heritage material, as they were long valued by ancient peoples as a raw material for producing stone tools and ornaments. In this perspective, geochemical, magnetic and spectroscopic fingerprinting has been much used to find the sources of obsidian archaeological materials (Shackley, 2005).

Obsidians have an unusual black to brown color in hand specimen. This color is different from the specific color range of Fe-containing synthetic silicate glasses, showing a blue to green and yellow color as a function of the redox conditions (Calas et al., 2020). In addition, obsidians show exotic optical effects such as light diffraction and iridescence (Ma et al., 2001 and 2007). The color of obsidians is usually qualitatively assessed by a visual observation, and the optical spectroscopic grounds of the dark brown to black color of obsidian have received a limited attention (Ma et al., 2007). Spectroscopic studies of iron speciation in obsidian include Mössbauer and EPR spectroscopies (e.g., Regnard et al., 1981; Schmidbauer et al., 1986; Duttine et al., 2003) and, more recently, Raman microspectrometry (Di Genova et al., 2018). They show the coexistence of diluted  $\text{Fe}^{3+}$  in the glassy matrix with magnetite nanolites and Fe-rich domains at the origin of the magnetic properties of obsidians (Ferk et al., 2011). However, a relation between this diversified iron speciation and the coloration of obsidian has not yet been established. In line with the diversity of Fe-surroundings, the presence of nanometer-sized phases, referred to as nanolites, demonstrates the existence of a nano-scale organization in these volcanic glasses (Sharp et al., 1996). Nanolites have been recognized in a broad range of volcanic products through microscopic or spectroscopic approaches (Di Genova et al., 2017 and 2018; Mujin and Nakamura, 2020). Recently, they were suggested to play a significant role in volcanic processes, being suspected to affect the transition from effusive to explosive regime (Caceres et al., 2020) by nucleating the growth of gas bubbles.

We use a combination of optical absorption and EPR spectroscopic measurements at room and low temperature to show the incidence of the complex Fe-speciation in obsidians on their unique optical properties, which are clearly distinct from those of synthetic Fe-bearing silicate glasses. Most Fe sites are not diluted in the structure of the rhyolitic glass, but occur in mixed valence, magnetite-like clusters, responsible for the black coloration of obsidians through electron hopping. As far as Fe speciation is concerned, the name of obsidian is

not synonymous of rhyolitic glass. These well-defined molecular topologies may represent the precursors (nuclei?) of the (ultra)nanolites detected in silicic volcanic glasses, being unique witnesses, at a molecular-scale, of the undercooling associated to extensive degassing in the rising magma. However, such diversity raises questions about the significance of redox values in these complex materials.

## **2. Materials and analytical methods**

### *2.1 Samples*

The studied obsidian samples were selected from two kinds of formations: silicic domes and obsidian clasts from high-silica rhyolitic tuffs. The former include rhyolitic obsidians from (i) the top and the rim of the Panum Dome, samples #1 and 2, respectively (part of the ca. 1340 A.D. eruption of the Mono Craters chain, Ca, USA; Befus et al., 2015), (ii) the Roche Rosse Rhyolite on the northeastern coast of Lipari (Eolian Islands, Italy) erupted at 730 A.D. (Bullock et al., 2018), (iii) Bombarda (Milos Island, Cyclades, Greece), dated at 1.47Ma (Arias et al., 2006), (iv) Sierra de Guamani (Cordillera Real, Ecuador) (Santi et al., 2010) dated at 0.18 Ma (Bellot-Gurlet et al., 1999). The latter, often named “Apache tears”, come from Cochiti, Kasha-Katuwe Tent Rocks National Monument, located on the east side of the Peralta canyon, Bearhead Rhyolitic tuff, Jemez volcanic field (NM, USA) and dated at  $\approx 6.75\text{--}7.0$  Ma (Shackley et al., 2016). These aphyric obsidians are X-ray amorphous (more than 95% glass) without indication of the presence of crystalline magnetite. Two Fe-bearing synthetic glasses were used for comparison, a soda-lime silicate glass and a diopside glass, melted in air at 1200 and 1450°C, respectively. Electron probe microanalysis was used to determine the obsidian composition using a defocused beam of 15  $\mu\text{m}$  (Cameca Camebax, Camparis platform, Sorbonne University, France). A 15 kV voltage with a 40 nA beam current were used. X-ray intensities were corrected for dead-time, background and matrix effects using the PAP correction procedure (Pouchou and Pichoir 1985). The composition of the samples is given in Table 1.

### *2.2 Variable temperature optical absorption spectroscopy*

Optical absorption spectra were obtained using a double beam computerized Perkin-Elmer Lambda 1050 spectrophotometer (IMPMC spectroscopy platform) with a 4×4 mm beam size on thin sections polished both sides, with a thickness of 1 to 3 mm size depending on the intensity of the color of the sample. The spectra were recorded in transmission mode between 4,500 cm<sup>-1</sup> (2,200 nm) and 30,000 cm<sup>-1</sup> (330 nm) in the near UV-visible-near IR range at ambient temperature (293K). A He-cryostat under vacuum (around 3.4×10<sup>-7</sup>mbar) was used to record low temperature spectra (10K). After correction for reflection on the polished faces, the absorption spectra were normalized to the sample thickness. The spectral resolution varies from 0.8 nm in the UV region to 2 nm in the near IR - visible region.

### *2.3 Variable temperature EPR spectroscopy*

EPR spectra were collected between room temperature and 80K at 9.4 GHz with a Bruker ESP300E using a modulation amplitude of 1 G, a modulation frequency of 100 KHz, and a microwave power of 40 mW. The comparison among the investigated samples is enabled by measurements being performed in calibrated Suprasil® grade silica tubes and a constant filling factor of the cavity. EPR X-band spectra were normalized to sample mass, gain, amplitude modulation and square root of microwave power (in mW).

## **3. Results**

### *3.1 Characteristics of the investigated obsidians*

The investigated calc-alkaline obsidians show a wide range of colors, from clear brown to black. The samples from Lipari, Milos and Mono Craters are translucent, black in hand specimen and will be referred to as black obsidians. The samples from Cochiti and Ecuador appear clear, transparent and slightly brown and will be referred to as clear brown obsidians. Two other samples of clear brown and transparent obsidians from New Mexico and Oregon have been used for comparison.

The polished slices of black obsidians, used for optical spectroscopic measurements, appear dark gray and heterogeneous with micro- to millimeter size microlites of feldspar, pyroxene, quartz and cristobalite that are dispersed in the vitreous matrix or concentrated in lines and bands of inclusions. Micrometric Fe oxide minerals are highly reflective. The glassy matrix of all the samples is chemically homogeneous with numerous bubbles.

By contrast, clear obsidians appear homogeneous and light brown. Obsidian chemistry is relatively constant whatever the provenance. The total amount of alkalis, between 8 and 9 wt.%, and of aluminum, about 13wt.%, indicates calc-alkaline compositions. The Fe-content of these glasses reported as FeO varies from 1 to 1.7 wt.% in the black obsidians to a constant value of about 0.5% in the clear brown ones (Table 1). Raman spectra (using a Renishaw InVia Raman microspectrometer equipped with 532nm and 785nm lasers) did not evidence the characteristic contribution of magnetite at  $670\text{ cm}^{-1}$  (Di Genova et al., 2018).

### *3.2 Optical absorption spectra of obsidians*

#### *3.2.1 Presentation of the obsidian spectra*

In silicate glasses, ferrous and ferric ions give rise to characteristic features in the UV-visible-near infrared spectra, which have been much investigated due to their interest in domains ranging from the exploration of Lunar and planetary surfaces (Bell et al., 1976; Cannon et al., 2017) to technological applications (Uchino et al., 2000; Galois, 2006). As in minerals, the contribution of the two Fe redox states to the optical absorption spectra occurs in different spectral domains, in the near infrared for  $\text{Fe}^{2+}$  and visible-near UV for  $\text{Fe}^{3+}$ , with a transmission window in between that is responsible for the peculiar blue-green color of these glasses (Galois, 2006). Additionally, a charge transfer band causes an absorption rise in the UV above  $27,000\text{ cm}^{-1}$  (Uchino et al., 2000).

These typical features are illustrated by the optical absorption spectra of Fe-containing diopside and soda-lime glasses (**Fig. 1**). In these two glasses, the main  $\text{Fe}^{2+}$  absorption band near  $9,000\text{ cm}^{-1}$  is broad, with a full width at half maximum (FWHM) of about  $6,000\text{ cm}^{-1}$  (Calas and Petiau, 1983; Jackson et al., 2005), a value much larger than in minerals ( $1,000\text{-}3,000\text{ cm}^{-1}$ ; Burns, 1993). This means that  $\text{Fe}^{2+}$  absorption extends beyond the range observed for octahedrally coordinated  $\text{Fe}^{2+}$  (Vercamer et al., 2016) and implies other coordination states. As in most  $\text{Fe}^{2+}$ -bearing glasses, this band shows an additional shoulder near  $5,500\text{ cm}^{-1}$ , which has been interpreted as arising from tetrahedral  $\text{Fe}^{2+}$  (Calas and Petiau, 1983; Uchino et al., 2000; Jackson et al., 2005), though an absorption at this position may also be an indication of 5-coordinated  $\text{Fe}^{2+}$  (Vercamer et al., 2016). By contrast, the speciation of  $\text{Fe}^{3+}$  is different in these two kinds of glasses: as the spectrum of the soda lime glass shows the characteristic absorption bands of tetrahedral  $\text{Fe}^{3+}$  as in other soda-lime glasses (Vercamer et al., 2016), in the

diopside glass, the  $\text{Fe}^{3+}$  optical transitions are hardly visible, being obscured by the oxygen to metal charge transfer band, as in other Fe-bearing glasses (Bingham et al., 1999).

The obsidian spectrum is different from that of the Fe-bearing glasses (**Fig. 1**). The distinctive features of the obsidian optical absorption spectra have been investigated in dark and clear obsidians, which show similar features in terms of spectral background and peak position (**Figs. 2a and 2b**). In the near infrared, at  $8,700\text{ cm}^{-1}$ , the  $\text{Fe}^{2+}$  absorption band is significantly narrower than that of  $\text{Fe}^{2+}$  in silicate glasses, with a full width at half maximum of  $4,000\text{ cm}^{-1}$ . The feature near  $4,500\text{ cm}^{-1}$  is almost absent. In the visible domain, the transmission window of the Fe-bearing glasses between  $14,000$  and  $22,000\text{ cm}^{-1}$  is obscured in the obsidian spectrum by a broad absorption band around  $18,000\text{ cm}^{-1}$ , with two superimposed features at  $18,100$  and  $20,500\text{ cm}^{-1}$ . Crystal-field  $\text{Fe}^{3+}$  bands near  $26,500$ ,  $24,000$  and  $22,500\text{ cm}^{-1}$  are at the same position as in the soda lime glass, but with a smaller relative intensity, in relation with different Fe-redox states. The high redox value of Fe ( $\text{Fe}^{3+}/\text{Fe}^{\text{tot}} = 0.8$ ) in the soda-lime glass explains the high intensity of the  $\text{Fe}^{3+}$  absorption bands, relative to the more reduced redox state of Fe in the Lipari obsidian ( $\text{Fe}^{3+}/\text{Fe}^{\text{tot}} = 0.1$ ) (Regnard et al., 1981; Spiering and Seifert, 1985).

### 3.2.2 The origin of the obsidian spectral features

The optical spectrum of obsidians exhibits a residual absorption at  $5,000\text{ cm}^{-1}$ , responsible for the characteristic grey to black color of obsidians. This background is lower for clear brown obsidians than for black ones. Another cause of light absorption corresponds to a Rayleigh scattering increasing with increasing wavenumbers. This light scattering by micro-heterogeneities (microlites, bubbles, fractures...) makes the obsidian translucent and not transparent, by contrast to synthetic glasses. The abruptly changing slope of the absorption beyond  $25,000\text{ cm}^{-1}$  illustrates the third kind of background absorption. It is due to the additional background absorption by the low wavenumber tail of an intense Gaussian-shaped oxygen to metal charge transfer (OMCT) band ( $\text{O}^{2-} \rightarrow \text{Fe}^{3+}$  and  $\text{O}^{2-} \rightarrow \text{Fe}^{2+}$ ) similar to that observed in Fe-bearing silicate glasses (Uchino et al., 2000; Vercamer et al., 2015). The absorption bands of obsidians superimposed to this background absorption are more complex than in synthetic glasses and can be divided into four domains.

- First, the bands related to molecular water and hydroxyl groups may be seen in the near infrared at about  $5,200$ ,  $4,500$ , and  $4,050\text{ cm}^{-1}$ , superimposed on the tail of the fundamental OH stretching vibration band at  $3,570\text{ cm}^{-1}$ . These bands have been widely investigated in natural and synthetic glasses (e.g. Newman et al., 1986; Behrens and Nowack, 2003; Balzer et al., 2020) to get information on the speciation of OH and  $\text{H}_2\text{O}$  in magmas (Mysen



and Richet, 2019). In the investigated obsidians, the total water content ranges between 0.46% in the Cochiti  
marekanite up to 1.3% in the Panum Dome #2 obsidian. The peak at  $4,500\text{ cm}^{-1}$  is related to a combination mode  
of stretching of Si-OH and Al-OH groups. The small peak at  $5,200\text{ cm}^{-1}$  corresponds to the combination of  
stretching and bending modes of  $\text{H}_2\text{O}$  molecules. The peak at  $7,100\text{ cm}^{-1}$ , which represents the first overtone of the  
OH-stretching vibration originating from both  $\text{H}_2\text{O}$  molecules and Si-OH groups, is partly superimposed on the  
 $\text{Fe}^{2+}$  band of obsidians.

- Second, a symmetrical band is located at  $8,700\text{ cm}^{-1}$  and dominates the absorption spectra of obsidians. It has a  
pure Gaussian shape in clear brown obsidians (**Fig. S1**), whereas a second minor Gaussian component must be  
added to fit the band in the black ones (**Fig.S2**). Its intensity shows a qualitative variation with the Fe-content of  
the sample and is higher in black than in clear brown obsidians. The full width at half maximum of this band is  
constant in all spectra (about  $4,000\text{ cm}^{-1}$ ). This band may be related to a transition of octahedral  $\text{Fe}^{2+}$ . Its spectral  
properties (mostly position and shape) are original relative to those observed in minerals (Burns, 1993). Such a  
symmetrical shape is not observed in synthetic Fe-bearing glasses and will be further discussed in 4.1. The Lipari  
and Milos obsidian spectra show a shoulder at  $5,500\text{ cm}^{-1}$  that is not observed in the other obsidian spectra. In  
minerals, this position is usually indicative of tetrahedral  $\text{Fe}^{2+}$  (Burns, 1993).

- Third, a large, weak and complex band extending between  $13,000$  and  $22,000\text{ cm}^{-1}$  occurs in the spectra of both  
types of obsidians, with small features superimposed at  $18,100$  and  $20,300\text{ cm}^{-1}$ . The spectral bandwidth of this  
band is large (about  $6,000\text{ cm}^{-1}$ ). As the  $8,700\text{ cm}^{-1}$  band, this original band at  $18,300\text{ cm}^{-1}$  is not found in synthetic  
silicate glasses. Considering the width of this band, it can be attributed to a transition related to an Inter-Valence  
Charge Transfer (IVCT) process (see 4.3).

- The fourth component, above  $22,000\text{ cm}^{-1}$ , is related to the local environment of  $\text{Fe}^{3+}$  in the glass and comprises  
the intense cutoff due to the (Fe-O) OMCT (Uchino, 2000; Vercamer et al., 2015). Weak contributions are  
observed above  $22,000\text{ cm}^{-1}$ , being well-defined in the spectra of black obsidians, but only faintly visible in the  
spectra of the clear brown ones. These bands are related to spin-forbidden crystal-field transitions of tetrahedral  
 $\text{Fe}^{3+}$  at  $26,500\text{ cm}^{-1}$  (field-independent  ${}^6\text{A}_{1g} - {}^4\text{E}_g({}^4\text{D})$  transition) and at  $24,000$  and  $22,500\text{ cm}^{-1}$  (split  ${}^6\text{A}_{1g} - {}^4\text{T}_{1g}$ ,  
 ${}^4\text{E}_g({}^4\text{G})$  transition). Similar transitions of tetrahedral  $\text{Fe}^{3+}$  are observed in soda lime glasses and other Na-bearing  
silicate glasses (Vercamer et al., 2015). The small additional peaks at  $18,100$  and  $20,300\text{ cm}^{-1}$  may be also related  
to tetrahedral  $\text{Fe}^{3+}$ . Their intensity seems to be correlated to the evolution of intensity of the small tetrahedral  $\text{Fe}^{3+}$   
contributions at  $22,500$  and  $24,000\text{ cm}^{-1}$  as in orthoclase (Hofmeister and Rossman, 1984).

### 3.2.3 Low $T$ spectra

The 8,700  $\text{cm}^{-1}$  band and the background absorption remain unchanged between ambient  $T$  and 10K. But the optical absorption spectra exhibit in the visible and UV domains two major changes at low temperature (10K) (**Fig. 3**). The intensity of the complex structure between 14,000 and 22,000  $\text{cm}^{-1}$  in the spectra of the black obsidians increases dramatically (**Fig. 3a**), reaching  $\sim 1/3$  of the intensity of the 8,700  $\text{cm}^{-1}$  band in the Panum Dome #2 obsidian. In the spectra of the clear brown obsidians, this increase results in a higher absorbance than that of the 8,700  $\text{cm}^{-1}$  band (**Fig. 3b**). The shape of the band changes too, with a maximum at 18,300  $\text{cm}^{-1}$  in both types of obsidians. Considering the large width of this band and the wavenumber value of the IVCT that is higher than the 12,000-16,000  $\text{cm}^{-1}$  range of the  $\text{Fe}^{2+} \leftrightarrow \text{Fe}^{3+}$  IVCT in minerals (Rossman and Ehlmann, 2019), the additional contribution of a  $\text{Fe}^{2+} \leftrightarrow \text{Ti}^{4+}$  IVCT may be suspected. At the same time, the UV absorption edge shifts towards higher wavenumbers at low temperature, a more pronounced shift in black than in clear brown obsidians. Though the absorption edge retains the same slope, this may indicate a difference in the nature of the OMCT (**Figs. 3a and 3b**).

### 3.3 EPR spectroscopy

Electron Paramagnetic Resonance (EPR), also called Electron Spin Resonance (ESR), provides unique information on the local structure of glasses containing paramagnetic ions diluted in the glass matrix and the associated ferro- and ferri-magnetic phases and crystalline or amorphous superparamagnetic clusters (Calas, 1988). EPR is essentially sensitive to  $\text{Fe}^{3+}$  and  $\text{Mn}^{2+}$ , as  $\text{Fe}^{2+}$  has a too short magnetic relaxation time to be detected. Due to the great variability of the shape of the spectra, EPR is used to trace the source of obsidian artifacts (Duttine et al., 2003 and 2008). Early EPR studies of obsidians (Regnard et al., 1981; Calas and Petiau, 1983) recognized the presence of several species including superparamagnetic Fe-clusters and paramagnetic isolated  $\text{Fe}^{3+}$  ions. These spectra (**Fig. 4**) are different from those of synthetic glasses obtained by melt quenching showing the presence of  $\text{Fe}^{3+}$  ions diluted in the diamagnetic glass, with signals at 850, 1500 and 3200 G (Vercamer et al., 2015). In synthetic glasses, three  $\text{Fe}^{3+}$  contributions are observed (**Fig. 4**), the relative intensity of which depends on the rhombic or axial nature and intensity of the distortion of the  $\text{Fe}^{3+}$  site (not discussed here). At room temperature, the EPR spectra of obsidians are characterized by a broad and intense signal linked to superparamagnetic and other magnetic

clusters corresponding to Fe-concentrated domains, above which are superimposed weaker narrow signals of paramagnetic (isolated)  $\text{Fe}^{3+}$  (**Fig. 5**) The shape of these EPR signals remains similar in the various obsidians, with the noticeable exception of Panum Dome #2 obsidian (see below). In addition, their intensity does not vary much among the samples, the Lipari obsidian showing the highest relative concentration of paramagnetic  $\text{Fe}^{3+}$ , despite it having the lowest  $\text{Fe}^{3+}$  content.

The EPR data obtained at low temperature (down to 77K) are markedly different. In all obsidians samples, the super-paramagnetic contribution decreases sharply at low temperature, indicating the presence of nanoscale magnetic domains (**Figs 5 and 6a**). Indeed, the superparamagnetic domains adopt a ferro- or ferri magnetic behavior at low temperature, the temperature of transition from superparamagnetism to ferro/ferrimagnetism depending on the size and nature of these clusters. The spectacular variations between the spectra recorded at room and low temperature underline the importance of magnetic couplings involving  $\text{Fe}^{3+}$  ions in obsidians. By contrast, the intensity of the isolated  $\text{Fe}^{3+}$  signals increases with decreasing temperature T, following a Curie's law in  $T^{-1}$  that characterizes their paramagnetic behavior.

The superparamagnetic contribution largely dominates the EPR spectrum of the Panum Dome #1 of the Mono Crater, which gives a spectrum different from the other obsidian from Mono Crater, Panum Dome #2; however, the EPR spectrum of the glass obtained by quenching this obsidian melted at 1200 ° C for one hour shows the disappearance of these domains and the concomitant increase of the intensity of the diluted  $\text{Fe}^{3+}$  signal (near 1500 G) (**Fig. 6b**). This observation indicates that these clusters are characteristic of a slow cooling: remelting the glass easily dissolves the superparamagnetic clusters and the corresponding signals loose intensity. This behavior is the same as that of nanolites, showing that the formation of these clusters results from the fact that melt diffusivity decreases in a cooling dehydrated melt, as observed in silicic melts (Mujin et al., 2017).

Among the investigated obsidians, the EPR spectrum of marekanite shows only a minor variation of the superparamagnetic contribution at 77K, which indicates a low blocking temperature of these domains due to their small size. This is consistent with a faster quenching in rhyolitic tuffs than in effusive domes. Finally, the Panum Dome #2 sample shows an original spectrum different from what is expected in the case of  $\text{Fe}^{3+}$  ions in glasses. In particular, the signal at 1,500G is quite symmetrical, which is not observed for  $\text{Fe}^{3+}$  in silicate glasses. The similarity of the spectra obtained at room temperature and at low temperature indicates a low content of magnetic / superparamagnetic clusters involving  $\text{Fe}^{3+}$ . This original spectrum indicates a partial location of  $\text{Fe}^{3+}$  in an organized local structure with a low concentration of  $\text{Fe}^{3+}$  ions, making it possible to preserve the paramagnetic character of  $\text{Fe}^{3+}$  ions. The EPR spectra of some  $\text{Fe}^{3+}$ -doped spinels (Pathak et al., 2014) show

some similarities with the Panum Dome #2 obsidian spectrum. It is interesting to note in a few samples (marekanite, obsidians from Ecuador and New Mexico) the presence of  $\text{Mn}^{2+}$  diluted in the vitreous matrix, recognizable thanks to a characteristic hyperfine structure. In the other samples, the absence of this characteristic structure indicates that  $\text{Mn}^{2+}$  is incorporated in the magnetic clusters.

## 4. Discussion

### 4.1 Evidence of an ordered $\text{Fe}^{2+}$ environment linked to magnetite clusters

The optical spectra of Fe-containing synthetic glasses show an intense, broad, non-Gaussian and asymmetric band, with a maximum at 9,000-10,000  $\text{cm}^{-1}$  (**Fig. 1**) arising from  $\text{Fe}^{2+}$  sites diluted in the glass structure. This band has a large full width at half maximum (FWHM), about 8,000  $\text{cm}^{-1}$ , and extends over a large part of the visible spectrum. The shape of this asymmetric band is a result of a  $\text{Fe}^{2+}$  site distribution between 4- and 5-coordination, with only a minority of 6-fold coordinated  $\text{Fe}^{2+}$  (Jackson et al., 2005, Rossano et al., 2008). This site distribution depends on glass composition and explains the variability of the optical properties of  $\text{Fe}^{2+}$  in glasses. By contrast, all obsidian spectra show a well-defined  $\text{Fe}^{2+}$  band at the same position, 8,700  $\text{cm}^{-1}$ . This band has a constant FWHM of about 4,000  $\text{cm}^{-1}$ , i.e. half the width of the  $\text{Fe}^{2+}$  band in synthetic glasses (Uchino et al., 2000). This band remains unchanged at low temperature. Its shape is Gaussian in the light brown obsidians, but it incorporates a minor component on the high wavenumber in dark obsidians (**Figs. S.1 and S.2**). Such a peculiar absorption band has not been observed in silicate glasses. The low temperature optical spectra do not support an IVCT, which exhibits a strong temperature dependence (see 4.3). In addition,  $\text{Fe}^{2+}$ - $\text{Fe}^{3+}$  IVCT transitions occur at higher wavenumbers and give broad absorption bands (Burns, 1993). By contrast, the 8,700  $\text{cm}^{-1}$  band is narrower than the crystal field transitions of  $\text{Fe}^{2+}$  in glasses. Thus, the only alternative is a crystal-field transition of  $\text{Fe}^{2+}$  with a limited site distribution. The presence of just a single, unsplit  $\text{Fe}^{2+}$  absorption band indicates a regular or slightly distorted octahedral site. Any site distortion will result in split  $\text{Fe}^{2+}$  optical transitions, as observed in minerals (see Burns, 1993; Rossman, 2014; Vercamer et al., 2016). In addition, as  $\text{Fe}^{2+}$  is a  $d^6$  ion, it is subject to a dynamic Jahn-Teller effect that will also split the main optical transition of octahedral  $\text{Fe}^{2+}$  (Burns, 1993; Vercamer et al., 2016). This splitting may be observed if the dynamic distortion, which goes along with the Jahn-Teller effect of octahedral  $\text{Fe}^{2+}$ , is possible, as for  $[\text{Fe}(\text{H}_2\text{O})_6]^{2+}$  complexes or by a coupling

with the vibration modes of the matrix, as for  $\text{Fe}^{2+}$ -bearing MgO. Otherwise, the absence of splitting will result in only one crystal-field related transition.

The optical properties of magnetite-like clusters are at the origin of a  $\text{Fe}^{2+}$  absorption band similar to that which dominates the optical spectra of obsidians. In magnetite,  $\text{Fe}^{2+}$  occupies slightly distorted octahedral sites, which are not oriented along the vibration modes of the spinel structure.  $\text{Fe}^{2+}$  gives rise to a crystal field transition at  $7,200\text{ cm}^{-1}$ , with a minimal absorption near  $12,500\text{ cm}^{-1}$  and a bandwidth of about  $4,000\text{ cm}^{-1}$  (Wang and Qu, 2013; Taketomi et al., 1991). It retains a temperature independence of both the band position and intensity. The position of the absorption band is sensitive to the size of the nanomagnetite particles, shifting slightly towards higher wavenumbers with decreasing particle size in the nm range (Taketomi et al., 1991). The  $1,500\text{ cm}^{-1}$  difference with the value observed in obsidians would indicate the presence of magnetite-like clusters rather than magnetite nanolites. The unusual intensity of this octahedral  $\text{Fe}^{2+}$  band, also detected in the magnetite-chromite spinel solid solution, has been suggested to result from exchange-coupled pairing (Scafetta et al., 2020). In Mössbauer spectroscopy, these magnetite-like clusters give a symmetric quadrupole doublet characteristic of a superparamagnetic behavior, as shown by 7 nm-size magnetite nanoparticles (Si et al., 2004). By contrast, larger (i.e.  $> 15\text{ nm}$ ) magnetite particles give rise to a magnetically separated sextet often observed in the Mössbauer spectra of obsidians at room or at low temperature (Regnard et al., 1981; Spiering and Seifert, 1985; Stewart et al., 2003). This is consistent with a 20 nm lower limit of the size of superparamagnetic magnetite (Wang and Qu, 2013).

However, the additional presence of  $\text{Fe}^{2+}$  in a glassy environment cannot be excluded, in particular when considering the Mössbauer spectroscopy of some black obsidians here investigated, as Lipari and Milos, which show low  $\text{Fe}^{3+}/\text{total Fe}$  values, 7-9% and 9.5%, respectively (Regnard et al., 1981; Spiering and Seifert, 1985; Schmidbauer, 1986; Stewart et al., 2003). Although the fitting procedure did not take into account the  $\text{Fe}^{2+}$  site distribution that has been demonstrated in silicate glasses (Levitz et al., 1980; Rossano et al., 1999 and 2008), these spectra show the contribution of a broad and asymmetric doublet, which is characteristic of  $\text{Fe}^{2+}$  in glasses (Rossano et al., 2008). As discussed above, the contribution of superparamagnetic magnetite clusters is a doublet, even at low temperature, due to their small size. The low velocity component of the Mössbauer signal of these doublets will merge. The high velocity component indicates that  $\text{Fe}^{2+}$  occupies different kinds of sites, some  $\text{Fe}^{2+}$  occurring in the glassy matrix (Spiering and Seifert, 1985). The Mössbauer spectra of Lipari and Milos obsidians show Fe to be in a valence state intermediate between  $\text{Fe}^{2+}$  and  $\text{Fe}^{3+}$  (Schmidbauer et al., 1986).

Reconciling the apparently contradictory results from optical absorption and Mössbauer spectroscopy needs to take into account the absorption coefficients of  $\text{Fe}^{2+}$ . The diversity of  $\text{Fe}^{2+}$  speciation in obsidians precludes the calculation of this parameter, but the nature of the acting optical processes is very different. In the case of isolated  $\text{Fe}^{2+}$  in a glass, the crystal field transitions are dipole forbidden and will remain of low intensity, as in minerals and glasses (Burns, 1993). By contrast, in the case of magnetite clusters, the optical transitions are enhanced by exchange-coupled pairing between the neighboring Fe-sites and are expected to dominate the optical spectrum.

Magnetite clusters seem to be the main actors in the  $\text{Fe}^{2+}$  optical signature of obsidians. Indeed, the efficient light absorption by magnetite precludes the magnetite micro- and nanolites to contribute to this  $\text{Fe}^{2+}$  signal: light transmission through a magnetite thin film 85 nm thick, drops down to 20% (Baghaie Yazdi et al., 2011). At 5 nm thickness, transmission raises to 80%, which means that only the smallest ultrananolites and the magnetite-like clusters will contribute to this  $\text{Fe}^{2+}$  absorption band in obsidians. The same reasoning holds for the IVCT discussed in 4.3.

#### 4.2 *The $\text{Fe}^{3+}$ environment*

The optical spectra of obsidians show the optical transitions of diluted tetrahedral  $\text{Fe}^{3+}$  (Vercamer et al., 2015), even in the most reduced obsidians such as Lipari and Milos. As in minerals (Hofmeister and Rossman, 1984), tetrahedral  $\text{Fe}^{3+}$  gives rise to a relatively intense band at 26,500  $\text{cm}^{-1}$ , with a characteristic double absorption feature at 24,000 and 22,500  $\text{cm}^{-1}$  and two weaker bands at 20,000 and 18,000  $\text{cm}^{-1}$ . By contrast, diluted octahedral  $\text{Fe}^{3+}$  has a diagnostic absorption band at 22,500  $\text{cm}^{-1}$ , which coincidentally superimposes to one of the contributions of tetrahedral  $\text{Fe}^{3+}$ . As the relative intensity of the 24,000 and 22,500  $\text{cm}^{-1}$  transitions does not change among obsidians and the optical transitions are more intense for tetrahedral  $\text{Fe}^{3+}$  than for dilute octahedral  $\text{Fe}^{3+}$ , the optical spectra are consistent with diluted  $\text{Fe}^{3+}$  being in tetrahedral coordination. This does not exclude some octahedral  $\text{Fe}^{3+}$  to be present in the mixed valence clusters responsible for the IVCT of obsidians, in which charge-transfer processes hide crystal-field transitions. The fact that the weak bands at 20,000 and 18,000  $\text{cm}^{-1}$  are not blurred by disorder effects, contrary to what is observed in glasses (**Fig. 1**), does not indicate the glassy matrix to be the only host of  $\text{Fe}^{3+}$ . This contribution of isolated  $\text{Fe}^{3+}$  also contributes to the EPR spectra. It is of interest that the Panum Dome #2 sample, showing an EPR spectrum partly arising from an ordered surrounding of  $\text{Fe}^{3+}$ , shows the best resolved contribution of  $\text{Fe}^{3+}$  on the optical spectra.

### 4.3 The mixed-valence, Fe-rich domains: magnetite-like clusters?

One of the key properties of the optical spectra of obsidians is the presence of the broad band near 18,000  $\text{cm}^{-1}$ . This band shows a complex shape, indicating the presence of different optical transitions. The spectacular intensity enhancement at low temperature demonstrates that it arises from an intervalence charge transfer (IVCT) between  $\text{Fe}^{2+}$  and  $\text{Fe}^{3+}$ . Such exceptional property has not been described previously in silicate glasses and defines a unique property of volcanic glasses relative to synthetic glasses. An IVCT necessitates an electron hopping between two cations in neighboring octahedral sites sharing edges. These clusters may correspond to clusters with a spinel structure hosting  $\text{Fe}^{3+}$  and  $\text{Fe}^{2+}$  as discussed in 4.1. Such  $\text{Fe}^{2+}$ - $\text{Fe}^{3+}$  IVCT transitions have been observed in synthetic spinels at all compositions of the spinel-hercynite solid solution, indicating the presence of ordered clusters within the spinel structure (Halenius et al., 2002).

Magnetite and magnetite-hercynite spinels show a  $^{[6]}\text{Fe}^{2+}$ - $^{[6]}\text{Fe}^{3+}$  IVCT transition near 14,500-15,500  $\text{cm}^{-1}$  (Fontijn et al., 1999; Halenius et al., 2002; Seki et al., 2005). In obsidians, the wavenumber at which the IVCT is observed is higher by 3,000  $\text{cm}^{-1}$  than this value. Similarly, the crystal-field transition of  $\text{Fe}^{2+}$  in obsidian occurs at a position higher by 1,500  $\text{cm}^{-1}$  than the value observed in magnetite (Taketomi et al., 1991). These differences show that the magnetite-like clusters do not possess the optical properties of magnetite, but may act as magnetite nuclei. These clusters were not detected on the Raman spectra of these obsidians using their signature at 670  $\text{cm}^{-1}$  (Di Genova et al., 2018), as the population of ultrananolites with a true magnetite structure may be too small to be detected in these Fe-poor obsidians. Such ordered nanoclusters are independent of the glass structure. They are responsible for the broad superparamagnetic EPR signal, characteristic of magnetic interactions within clusters, but not between clusters. The upper size limit of the superparamagnetic properties of magnetite particles is about 20 nm (Wang and Qu, 2013).

Even if the proportion of  $\text{Ti}^{4+}$  in obsidians is low (**Table 1**), the  $^{[6]}\text{Ti}^{4+}$ - $^{[6]}\text{Fe}^{2+}$  IVCT needs to be considered. From the Mössbauer spectroscopy data on Lipari obsidian (Regnard et al., 1981), it can be deduced that they contain only about 0.1%  $\text{Fe}^{3+}$ . This is not so different from the Ti-content (0.058%) if one considers that  $\text{Fe}^{3+}$  is also present in diluted sites of the coexisting glass structure. The Ti-Fe IVCT is often observed near 20,000  $\text{cm}^{-1}$ , which may explain the large width (6,000  $\text{cm}^{-1}$ ) of the complex band around 18,000  $\text{cm}^{-1}$ . However, a detailed variable temperature investigation is necessary to understand this complex IVCT structure, which is of great significance as it is present in all the calc-alkaline obsidians investigated.

A mixed-valence character is also revealed by a doublet characteristic of a Fe valence state intermediate between  $\text{Fe}^{2+}$  and  $\text{Fe}^{3+}$  in the Mössbauer spectra of Lipari and Milos obsidians (Schmidbauer et al., 1986). The pioneering studies of Regnard et al. (1981), based on low temperature Mössbauer spectra including in presence of an external magnetic field, demonstrated the presence of ultrafine (<5 nm) clusters of magnetite  $\text{Fe}_3\text{O}_4$  in Lipari obsidians. These clusters constitute, together with dilute  $\text{Fe}^{2+}$  and  $\text{Fe}^{3+}$ , 74% of the total absorption. They may be a precursor of magnetite nanolites at the molecular scale. However, early Fe K-edge EXAFS data on the Lipari obsidian (Calas and Petiau, 1983) demonstrated the presence of only a Fe-O contribution at 2.04 Å, close to the average Fe-O distance in magnetite (2.05 Å: Henderson et al., 2007), without any evidence of the presence of a second shell: the size of these Fe-based clusters in obsidian is not large enough to allow detection of a magnetite-like structural organization.

#### 4.4 The Fe-clustering process

Ferric iron plays an important role in the glass structure. For instance, neutron diffraction and numerical modeling show direct evidence of Fe clustering in glasses of jadeite-acmite composition even at 5 at.% Fe concentration (Weigel et al., 2008). If the majority of  $\text{Fe}^{3+}$  is in tetrahedral coordination, randomly distributed in the alumino-silicate network, some  $\text{Fe}^{3+}$  and most  $\text{Fe}^{2+}$  are 5-coordinated and cluster through preferential edge-sharing; this local organization allows intervalence charge transfer and electron hopping between neighboring  $\text{Fe}^{2+}$  and  $\text{Fe}^{3+}$ .  $\text{Fe}^{3+}$  may be stabilized in tetrahedral coordination only if appropriate charge compensation is available, once the local charge balance of tetrahedral  $\text{Al}^{3+}$  is ensured. This demonstrates that the sites needed to build a spinel structure are already present within the glass.

The transition to a (proto)crystalline organization may be considered using a model suggesting that  $\text{Fe}^{2+}$  is involved with local charge balance of neighboring tetrahedral  $\text{Fe}^{3+}$  (Spiering and Seifert, 1985). In the glass structure, the presence of edge-sharing chains with  $\text{Fe}^{2+}$  and  $\text{Fe}^{3+}$  will be a precursor of a spinel structure based on edge-sharing octahedral chains interconnected by corner-sharing tetrahedra. This requires that  $\text{Fe}^{2+}$  and  $\text{Fe}^{3+}$  change from 5- to 6-coordination. It has been speculated that a 5-coordinated site is a frustrated octahedron (Calas et al., 2014 and 2020), which can hardly exist in glasses as a result of the atomic motions that characterize silicate melts. In silicic melts, all O atoms are linked by strong Si-O covalent bonds to silicate tetrahedra. The viscous flow and atomic diffusion at high temperature will cause the motion of silicate groups, which will weaken bonds to cation sites. The connection of these cationic units to the incipient Fe-rich, mixed valence clusters described



above will progressively hinder such permanent local reorganization of the Fe-sites, which will be able to retain an octahedral coordination. These clusters may reflect a starting ordered structural organization around Fe, probably based on a limited Fe site population, being sufficiently optically active to be easily detected. They indicate a local rearrangement of the glass, and these clusters may be seen as precursors of a future nucleation/crystallization of magnetite (ultra)nanolites in this type of glasses. Their size is large enough to imply sufficient Fe-sites in the electron hopping processes that are at the origin of an efficient light absorption over all the visible range, responsible for the black color of obsidians.

#### 4.5 *Why are calc-alkaline obsidians black?*

All obsidians show an important residual absorbance, in addition to the various optical absorption processes, as crystal-field transitions and intervalence charge transfers, above discussed. This minimal absorbance varies among the samples even from the same location. It can be evaluated to be between 0.2 and 3.6  $\text{cm}^{-1}$  in the 5,000  $\text{cm}^{-1}$ , a region outside the main absorption bands and in which light scattering is minimal (but still contributes). These values correspond to a "grey level", characterizing obsidian darkness without any hue, as the absorbance is constant over the entire visible spectrum.

Magnetite has been recognized as a major phase constituting microlites and nanolites in volcanic glasses (Sharp et al., 1996; Di Genova et al., 2018; Mujin and Nakamura, 2020; Allabar et al., 2020). It is among the most efficient light absorbing minerals in the visible domain, owing to the small energy barrier of electron hopping from octahedral  $\text{Fe}^{2+}$  to neighboring octahedral  $\text{Fe}^{3+}$  that is comparable with the energy of the optical band gap, 0.2 eV or 1600  $\text{cm}^{-1}$  (Liu and Di Valentin, 2017). For this reason, the presence of magnetite has been qualitatively suspected for decades to give obsidians their black color, based on simple visual observations without any firm optical spectroscopic grounds. It is possible to evaluate this contribution by reference to transparent  $\text{Fe}_3\text{O}_4$  thin films (Baghaie Yazdi et al., 2011). An overall thickness of 85 nm corresponds to an absorbance of 0.7. As discussed in 4.1, particles of this size or larger will absorb most of the incident light. This means that only magnetite microlites and nanolites and the large ultrananolites will contribute to the black color of obsidians.

As the linear residual absorbance of dark obsidians ranges from 4 to 6  $\text{cm}^{-1}$  (**Fig. 2**), this corresponds to an overall thickness of the magnetite clusters ranging from 485 to 730 nm for a 1 cm thick obsidian. This gives a crude estimate of the relative volume of absorbing magnetite of  $5 \cdot 10^{-5}$  to  $7 \cdot 10^{-5}$ . By considering the density of

magnetite and rhyolitic glasses (5.1 and 2.3, respectively), we obtain a guess of 100-150 ppm Fe participating to the black coloration of obsidians. This assessment relies on a random distribution of nanomagnetites. However, this low concentration illustrates the exceptional optical properties of magnetite, showing that even minute quantities exert a dramatic influence on the aspect of these original materials.

## 5. Conclusion

Obsidian is not just a glass, as illustrated by the complex Fe-speciation revealed by spectroscopic studies: indeed,  $\text{Fe}^{2+}$  and  $\text{Fe}^{3+}$  ions are largely located outside the glass structure forming clusters that partly inherit some optical properties of nano-magnetite domains. This explains the unusual color of obsidians that do not show the diverse hues expected from the presence of  $\text{Fe}^{2+}$  and  $\text{Fe}^{3+}$  in glasses. The optical absorption in the visible increases dramatically at low temperature, with an amplitude that is not observed in synthetic silicate glasses. They indicate exchange-coupled pairing and  $^{[6]}\text{Fe}^{2+}\text{-}^{[6]}\text{Fe}^{3+}$  and/or  $^{[6]}\text{Fe}^{2+}\text{-}^{[6]}\text{Ti}^{4+}$  IVCT processes. The EPR spectra show the presence of superparamagnetic domains in addition to minority paramagnetic  $\text{Fe}^{3+}$ . Optical and EPR spectroscopic data are consistent with the presence of ordered clusters. However, much remains to be understood about these clusters, concerning their structure, quantitative importance or links with the (ultra)nanolites. The smallest magnetite-like clusters are transparent enough to contribute to the original absorption bands of obsidians. The largest ones will contribute to the formation of nanolites giving obsidians their black color. This study shows also that Fe-speciation in calc-alkaline obsidians does not reflect a magmatic history. Most Fe is not located within the glass structure and does not show a local topology that is quenched from the magma. This unusual Fe-speciation has implications regarding the significance of the redox state of iron in obsidians, in presence of several Fe-speciations inherited from different stages of the obsidian formation. Obsidians cannot be considered as quenched witnesses of the initial magma, at least as far as Fe is concerned.

On the small-sized side of the size distribution of crystal-like heterogeneities, from microlites to nanolites and ultrananolites, the ordered clusters evidenced in this study represent a precursor (nucleus?) between glass structure and magnetite ultrananolites. They demonstrate a progressive organization of Fe-based units, which reflects the cooling and degassing processes that occurred during magma emplacement followed by post-magmatic structural and chemical changes. The quantification of the spectroscopic characteristics of these unusual spectra will provide useful tools to model the emplacement of these silicic magmas.

**Acknowledgements**

We thank the organizers of the "Silicate Melt Workshops" at la Petite Pierre in the French Alsace for the continuous success, over several decades, of this warm and efficient meeting, held in a unique European surrounding. We are grateful to Florence Galea and Nicolas Tisserand for their help in the acquisition of spectroscopic data at low temperature. Glass analysis with the Cameca electron microprobe has been made possible through the CAMPARIS facility of Sorbonne University. The manuscript has been greatly improved by two anonymous reviewers.

**Declaration of competing interest**

The authors declare that they have no known competing financial interests or personal relationships that could have appeared to influence the work reported in this paper.

## Figure Captions

Figure 1. Comparison of the optical absorption spectra of the Lipari obsidian (in black), a soda-lime glass (in red) and a diopside glass (blue dashed). Vertical lines indicate that the weak  $\text{Fe}^{3+}$  transitions in the near-UV occur at the same position and that the  $\text{Fe}^{2+}$  absorption band in the near-IR is different in both glasses.

Fig. 2. (a) Black obsidians; (b) Clear brown obsidians. The obsidian samples present similar optical spectra in terms of band position, intensity and width. In the two types of obsidians, the absorption minimum is located at a remarkably constant position,  $14,000\text{ cm}^{-1}$  and  $13,000\text{ cm}^{-1}$  for the black and clear obsidians, respectively. This explains the constancy of the observed color. In (a), the true absorbance of the black obsidians has been kept. In (b), the spectra of Cochiti, New Mexico and Oregon obsidians have been shifted for clarity, retaining the same relative absorbance (the scaling of  $1\text{ cm}^{-1}$  is indicated for reference).

Fig. 3. Optical absorption spectra of Panum Dome #2 obsidian, black, and Cochiti, clear brown, obsidians at ambient T and 10K. The broad band centered at  $18,000\text{ cm}^{-1}$  is sharply intensified at 10K in both types of obsidians.

Fig. 4. Room temperature X-band EPR signal of  $\text{Fe}^{3+}$  in New Mexico obsidian and a Na-Ca silicate glass. The sharp signal near 1,500 G in the two glasses corresponds to diluted  $\text{Fe}^{3+}$ . The obsidian spectrum is characterized by a broad signal covering most of the magnetic field investigated, indicative of the presence of superparamagnetic clusters.

Fig. 5. Comparison of EPR spectra of obsidians recorded at room temperature and liquid nitrogen temperature (77 K). The broad contribution that affects the spectra at room temperature is much attenuated at low temperature, indicating of a superparamagnetic behavior created by Fe-rich clusters. The variability in the shape of the spectra arises from differences in the size and shape of these clusters. All spectra have been normalized to facilitate their comparison.

532 Fig. 6. EPR spectra of the Panum Dome #1 obsidian at room temperature and 10K (a) and after remelting in air  
533 (b). The spectrum of the remelted obsidian shows an enhancement of the diluted  $\text{Fe}^{3+}$  signal (near 1,500 G) and  
534 the disappearance of the superparamagnetic signal.

535

536 **Table Caption**

537

538 Table 1. Elemental composition of the obsidians investigated.

539

540

## References

- A. Allabar, E.S. Gross, M. Nowak. The effect of initial H<sub>2</sub>O concentration on decompression - induced phase separation and degassing of hydrous phonolitic melt *Contrib. to Mineral. Petrol.*, 2 (2020), pp. 1-19.
- A. Arias, M. Oddone, G. Bigazzi, A. Di Muro, C. Principe, P. Norelli. New data for the characterisation of Milos obsidians *J. Radioanal. Nuclear Chem.*, 268 (2006), pp. 371-386
- M. Baghaie Yazdi, M.-L. Goyallon, T. Bitsch, A. Kastner, M. Schlott, and L. Alff. Transparent magnetic oxide thin films of Fe<sub>3</sub>O<sub>4</sub> on glass. *Thin Solid Films*, 519 (2011), pp. 2531–2533.
- R. Balzer, H. Behrens, T. Waurischk, S. Reinsch, R. Müller, P. Kiefer, J. Deubener, M. Fechtelkord. Water in Alkali Aluminosilicate Glasses. *Front. Mater.*, 7 (2020), pp. 85.
- H. Behrens, M. Nowak. Quantification of water speciation in silicate glasses by IR spectroscopy — in situ vs. quench technique. *Phase Transit.*, 76 (2003), pp. 45-61.
- K.S. Befus, M. Manga, J.E. Gardner, M. Williams. Ascent and emplacement dynamics of obsidian lavas inferred from microlite textures. *Bull. Volcanol.*, 77 (2015), pp. 1-17.
- P. M. Bell, H. K. Mao, R.A. Weeks. Optical spectra and electron paramagnetic resonance of lunar and synthetic glasses: A study of the effects of controlled atmosphere, composition and temperature. *Proc. Lunar Sci. Conf. 7th* (1976), pp. 2543–2559.
- L. Bellot-Gurlet, G. Poupeau, O. Dorighel, Th. Calligaro, J.-C. Dran, J. Salomon. A PIXE/fission track dating approach to sourcing studies of obsidian artifacts in Colombia and Ecuador. *J. Archaeol. Sci.*, 26 (1999), pp. 855–860.
- P.A. Bingham, J.M. Parker, T. Searle, J.M. Williams, K. Fyles. Redox and clustering of iron in silicate glasses. *J. Non-Cryst. Solids*, 253 (1999), pp. 203-209
- L.A. Bullock, R. Gertisser, B. O'Driscoll. Emplacement of the Rocche Rosse rhyolite lava flow (Lipari, Aeolian Islands) *Bull. Volcanol.*, 80 (2018), p. 48.
- R.G. Burns. *Mineralogical Applications of Crystal Field Theory* (second ed.), Cambridge University Press, Cambridge (1993)
- F. Cáceres, F. B. Wadsworth, B. Scheu, M. Colombier, C. Madonna, C. Cimarelli, K-U. Hess, M. Kaliwoda, B. Ruthensteiner, D. B. Dingwell. Can nanolites enhance eruption explosivity? *Geology*. 48 (2020) 10.1130/G47317.1.

571 G. Calas. Electron paramagnetic resonance. *Rev. Mineral.*, 18 (1988), pp. 513-571.

572 G. Calas, L. Galois, L. Cormier, G. Ferlat, G. Lelong. The structural properties of cations in nuclear  
573 glasses. *Proc. Mater. Sci.*, 7 (2014), pp. 23-31.

574 G. Calas, L. Galois, L. Cormier. *Encyclopedia of Glass Science, Technology, History and Culture*, P.  
575 Richet Ed., The American Ceramic Society (2020) pp. 677-691.

576 G. Calas, J. Petiau. Structure of oxide glasses. Spectroscopic studies of local order and crystallochemistry.  
577 Geochemical implications. *Bull. Mineral.*, 106 (1983), pp. 33–55.

578 K. Cannon, J. Mustard, S. Parman, E. Sklute, M.D. Dyar, R. Cooper Spectral properties of Martian and  
579 other planetary glasses and their detection in remotely sensed data. *J. Geophys. Res. Planets* 122 (2017) pp. 249–  
580 268.

581 D. Di Genova, S. Kolzenburg, S. Wiesmaier, E. Dallanave, D. R. Neuville, K. U. Hess & D. B. Dingwell.  
582 A compositional tipping point governing the mobilization and eruption style of rhyolitic magma. *Nature*, 552  
583 (2017), pp.235–238

584 D. Di Genova, A. Caracciolo, S. Kolzenburg. Measuring the degree of "nanotilization" of volcanic glasses:  
585 understanding syn-eruptive processes recorded in melt inclusions. *Lithos*, 318 (2018), pp. 209-218

586 M. Duttine, G. Villeneuve, G. Poupeau, A.M. Rossi. Electron spin resonance of  $\text{Fe}^{3+}$  ion in obsidians from  
587 Mediterranean islands. Application to provenance studies. *J. Non-Cryst. Solids*, 323 (2003), pp. 193-199

588 M. Duttine, R.B. Scorzelli, G. Cernicchiaro, G. Poupeau, N. Guillaume-Gentil. Magnetic properties and  
589 electron spin resonance of Ecuadorian obsidians. Application to provenance research of archeological samples. *J.*  
590 *Magn. Mater.*, 320 (2008), pp. e136-e138

591 A. Ferk, R. Leonhardt, K.-U. Hess, D. Dingwell. Paleointensities on 8 ka obsidian from Mayor Island, New  
592 Zealand. *Solid Earth*, 2 (2011), pp. 259-270

593 W.F.J. Fontijn, P.J. Zaag, L.F. Feiner, R. Metselaar, M.A.C.J. Devillers. A consistent interpretation of the  
594 magneto-optical spectra of spinel type ferrites. *J. Appl. Phys.*, 85 (1999), pp. 5100-5105.

595 L. Galois. Structure-property relationships in industrial and natural glasses. *Elements*, 2 (2006), pp. 293-  
596 297.

597 U. Hålenius, H. Skogby, G.B. Andreozzi. Influence of cation distribution on the optical absorption spectra  
598 of  $\text{Fe}^{3+}$ -bearing spinel s.s.-hercynite crystals: Evidence for electron transitions in  $^{\text{VI}}\text{Fe}^{2+}$ - $^{\text{VI}}\text{Fe}^{3+}$  clusters. *Phys.*  
599 *Chem. Miner.*, 29 (2002), pp. 319-330.

600 C.M.B. Henderson, J.M. Charnock, D.A. Plant. Cation occupancies in Mg, Co, Ni, Zn, Al ferrite spinels: a  
601 multi-element EXAFS study. *J. Phys.: Condens. Matter*, 19 (2007), pp. 076214

602 A.M. Hofmeister, G.R. Rossman. Determination of Fe<sup>3+</sup> and Fe<sup>2+</sup> concentrations in feldspar by optical  
603 absorption and EPR spectroscopy. *Phys. Chem. Miner.*, 11 (1984), pp. 213-224

604 W.E. Jackson, F. Farges, M. Yeager, P.A. Marbrouk, S. Rossano, G.A. Waychunas, E.I. Solomon, G.E.  
605 Brown Jr. Multi-spectroscopic study of Fe(II) in silicate glasses: Implications for the coordination environment  
606 of Fe(II) in silicate melts, *Geochim. Cosmochim. Acta*, 69 (2005), pp. 4315–4332.

607 R. Leonhardt, J. Matzka, A.R.L. Nichols, D.B. Dingwell. Cooling rate correction for paleointensity  
608 determination for volcanic glasses by relaxation geospeedometry *Earth Planet. Sci. Lett.*, 243 (2006), pp. 282-  
609 292.

610 H. Liu, C. Di Valentin. Band Gap in Magnetite above Verwey Temperature Induced by Symmetry  
611 Breaking. *J. Phys. Chem. C.*, 121 (2017), pp. 25736-25742.

612 C. Ma, J. Gresh, G.R. Rossman, G.C. Ulmer, E.P. Vicenzi. Micro-analytical study of the optical properties  
613 of rainbow and sheen obsidians. *Can. Mineral.*, 39, (2001), pp.57-71.

614 C. Ma, G.R. Rossman, J.A. Miller. The origin of color in “fire” obsidian. *Can. Mineral.*, 45 (2007), pp.  
615 551-557.

616 M. Mujin, M. Nakamura, A. Miyake. Eruption style and crystal size distributions: crystallization of  
617 groundmass nanolites in the 2011 Shinmoedake eruption. *Am. Mineral.*, 102 (2017), pp. 2367-2380.

618 M. Mujin, M. Nakamura. Late-stage groundmass differentiation as a record of magma stagnation,  
619 fragmentation, and rewelding. *Bull. Volcanol.*, 82 (2020), p. 48.

620 B. Mysen B., P. Richet. *Silicate Glasses and Melts*, Second Edition (2019).

621 S. Newman, E.M. Stolper, E. Stolper. Measurement of water in rhyolitic glasses: calibration of an infrared  
622 spectroscopic technique. *Am. Mineral.*, 71 (1986), pp. 1527-1541.

623 N. Pathak, S.K. Gupta, K. Sanyal, M. Kumar, R.M. Kadam, V. Natarajan. Photoluminescence and EPR  
624 studies on Fe<sup>3+</sup> doped ZnAl<sub>2</sub>O<sub>4</sub>: an evidence for local site swapping of Fe<sup>3+</sup> and formation of inverse and normal  
625 phase. *Dalton Trans.*, 43 (2014), pp. 9313-9323.

626 J.L. Pouchou, F. Pichoir. Quantitative analysis of homogeneous or stratified microvolumes applying the  
627 model “PAP”. In: Heinrich, K.F.J., Newbury, D. (Eds.), *Electron Probe Quantitation*. Springer, US (1991), pp.  
628 31–75.



629 J.R. Regnard, F. Chavez-Rivas, J. Chappert. Study of the oxidation states and magnetic properties of iron in  
630 volcanic glasses: Lipari and Teotihuacan obsidians. *Bull. Mineral.*, 104 (1981), pp.204 – 210.

631 S. Rossano, E. Balan, G. Morin, J.P. Bauer, G. Calas, C. Brouder.  $^{57}\text{Fe}$  Mössbauer spectroscopy of tektites.  
632 *Phys. Chem. Miner.*, 26 (1999), pp. 530-538.

633 S. Rossano, H. Behrens, M. Wilke. Advanced analyses of  $^{57}\text{Fe}$  Mössbauer data of alumino-silicate glasses.  
634 *Phys. Chem. Miner.*, 35 (2008), pp. 77-93.

635 G.R. Rossman. Optical spectroscopy *Rev. Mineral. Geochem.*, 78 (2014), pp. 371-398.

636 G.R. Rossman, B.L. Ehlmann. Electronic Spectra of Minerals in the Visible and Near-Infrared Regions. In  
637 J. Bishop, J. Bell III, & J. Moersch (Eds.), *Remote Compositional Analysis: Techniques for Understanding*  
638 *Spectroscopy, Mineralogy, and Geochemistry of Planetary Surfaces* (Cambridge Planetary Science, 2019, pp. 3-  
639 20). Cambridge University Press.

640 A.C. Rust, K.V. Cashman. Multiple origins of obsidian pyroclasts and implications for changes in the  
641 dynamics of the 1300 B.P. eruption of Newberry Volcano, USA. *Bull. Volcanol.*, 69 (2007), pp. 825-845

642 P. Santi, A. Renzulli, M. Oddone. Increasing data (INAA) on Ecuadorian obsidian artifacts: preliminary  
643 provenance and a clue for pre-Columbian eastward trade. *J. Archaeol. Sci.*, 37 (2010), pp. 1753-1760.

644 M.D. Scafetta, T.C. Kaspar, M.E. Bowden, S.R. Spurgeon, B.E. Matthews S.A. Chambers. Reversible  
645 oxidation quantified by optical properties in epitaxial  $\text{Fe}_2\text{CrO}_{4+\delta}$  films on (001)  $\text{MgAl}_2\text{O}_4$ . *ACS Omega*, 7 (2020),  
646 pp. 3240–3249.

647 E. Schmidbauer, E. Mosheim, N. Semioschkina. Magnetization and  $^{57}\text{Fe}$  Mossbauer Study of Obsidians.  
648 *Phys. Chem. Miner.*, 13 (1986), pp. 256–261.

649 M. Seki, A.K.M. Akther Hossain, T. Kawai, H. Tabata. Photocontrol of magnetization in Al-substituted  
650  $\text{Fe}_3\text{O}_4$  thin films. *J. Appl. Phys.*, 97 (2005), p. 08354.

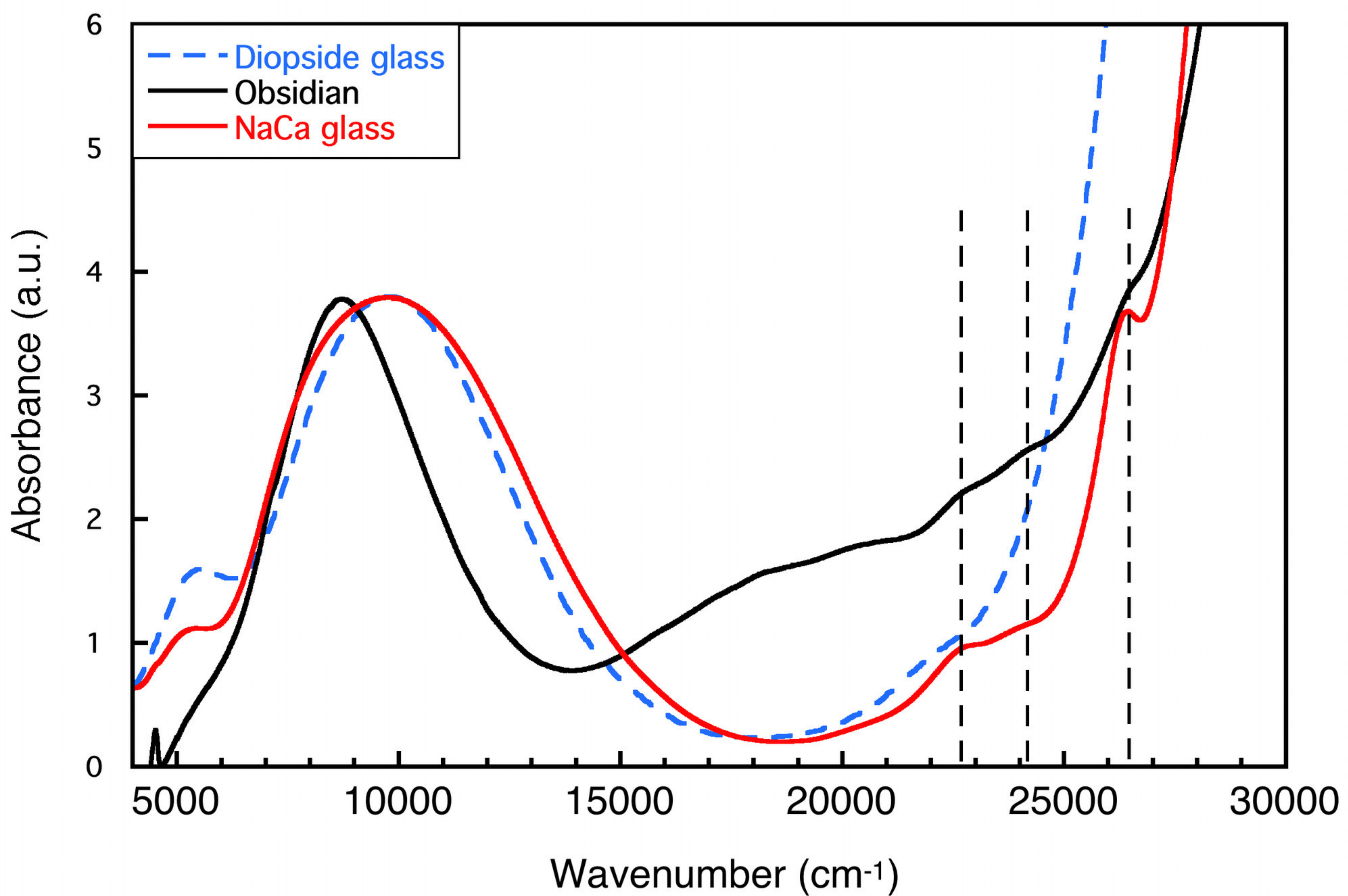
651 M. S. Shackley. *Obsidian: Geology and Archaeology in the North American Southwest*, University of  
652 Arizona Press, Tucson, 2005.

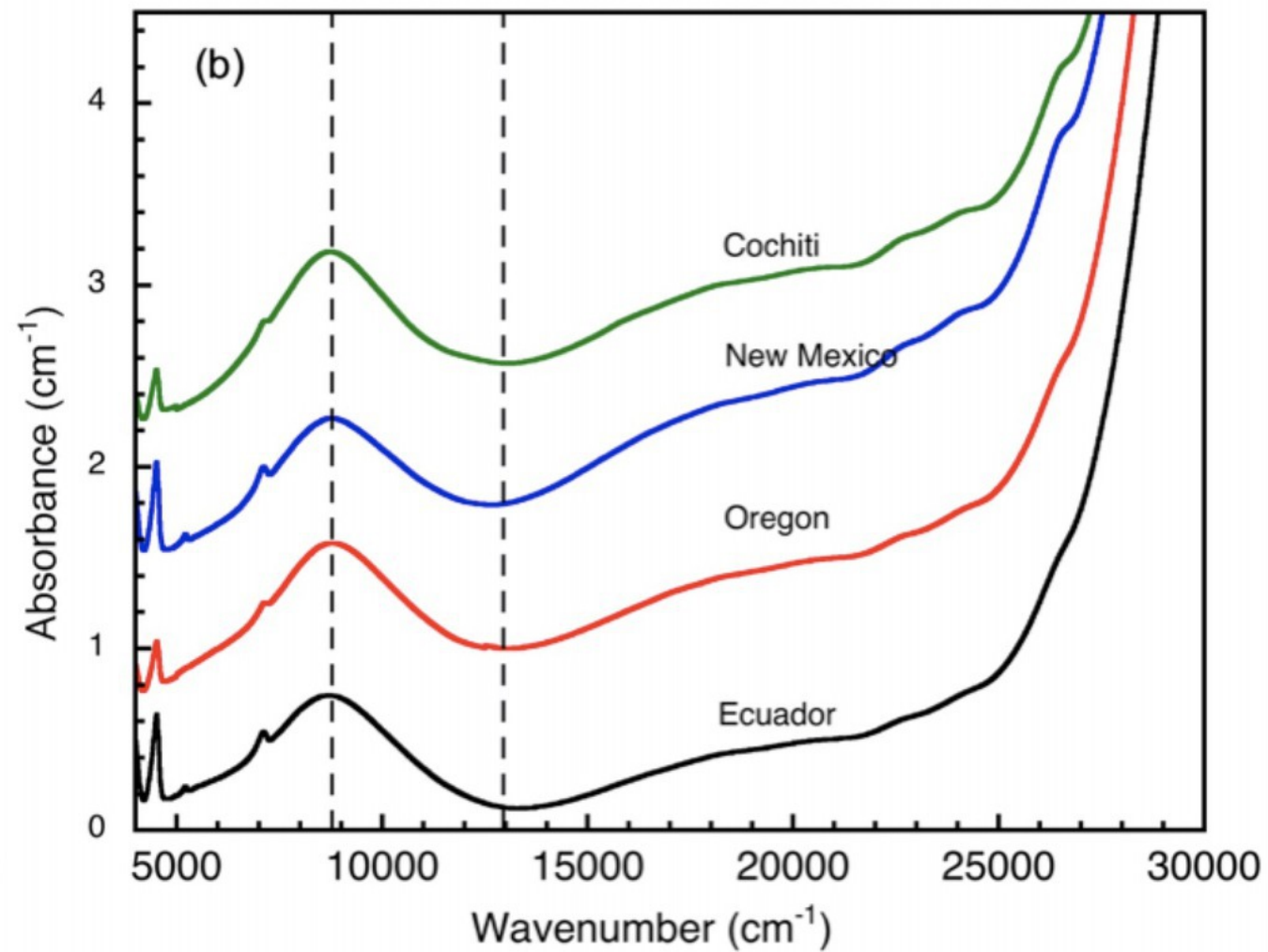
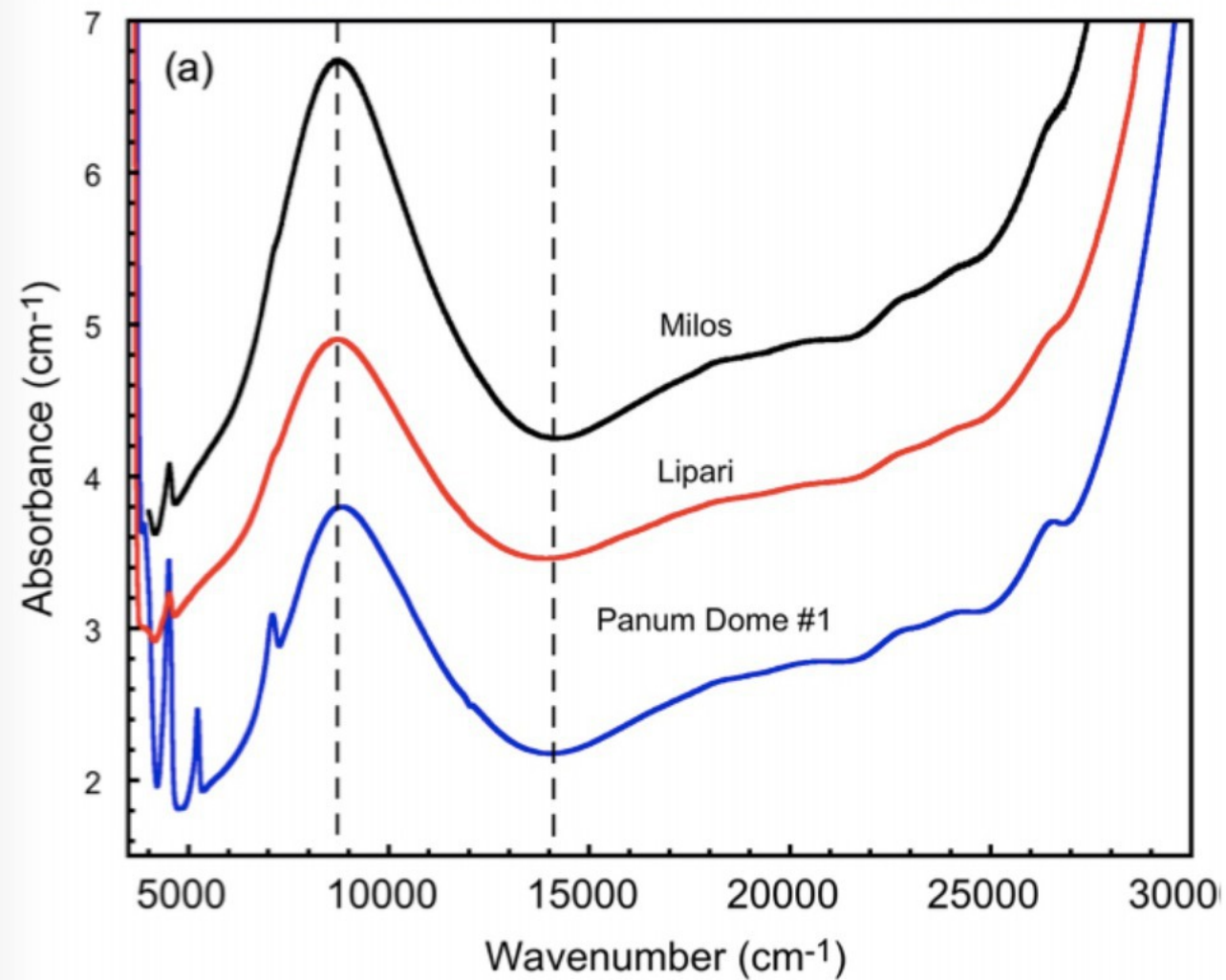
653 M. Shackley, F. Goff, S. Dolan. Geologic Origin of the Source of Bearhead Rhyolite (Paliza Canyon)  
654 Obsidian, Jemez Mountains, Northern New Mexico. *New Mexico Geology*, 38 (2016), pp. 52-65.

655 T.G. Sharp, R.J. Stevenson, D.B. Dingwell. Microlites and “nanolites” in rhyolitic glass: microstructural  
656 and chemical characterization. *Bull. Volcanol.*, 57 (1996), pp. 631–640.

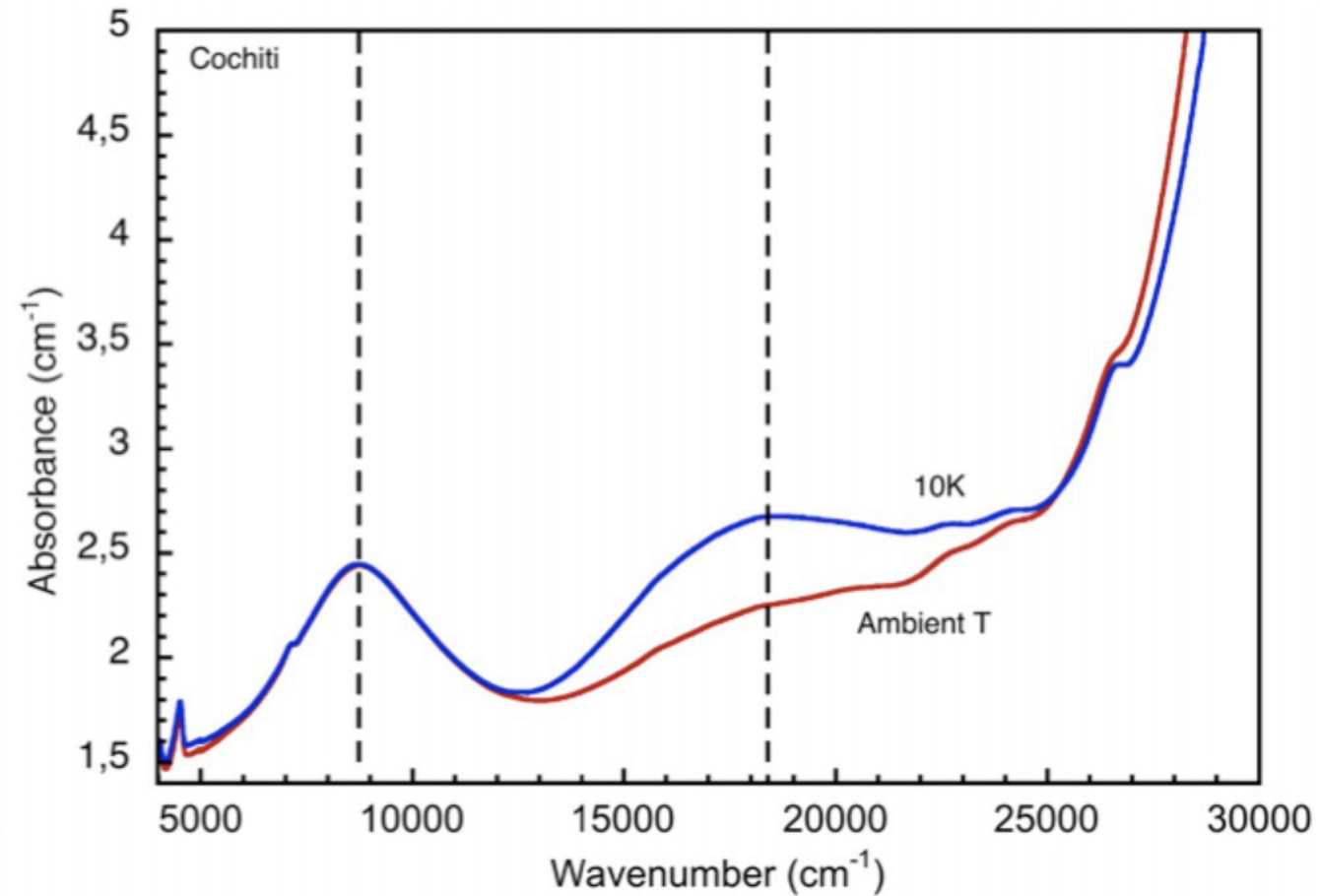
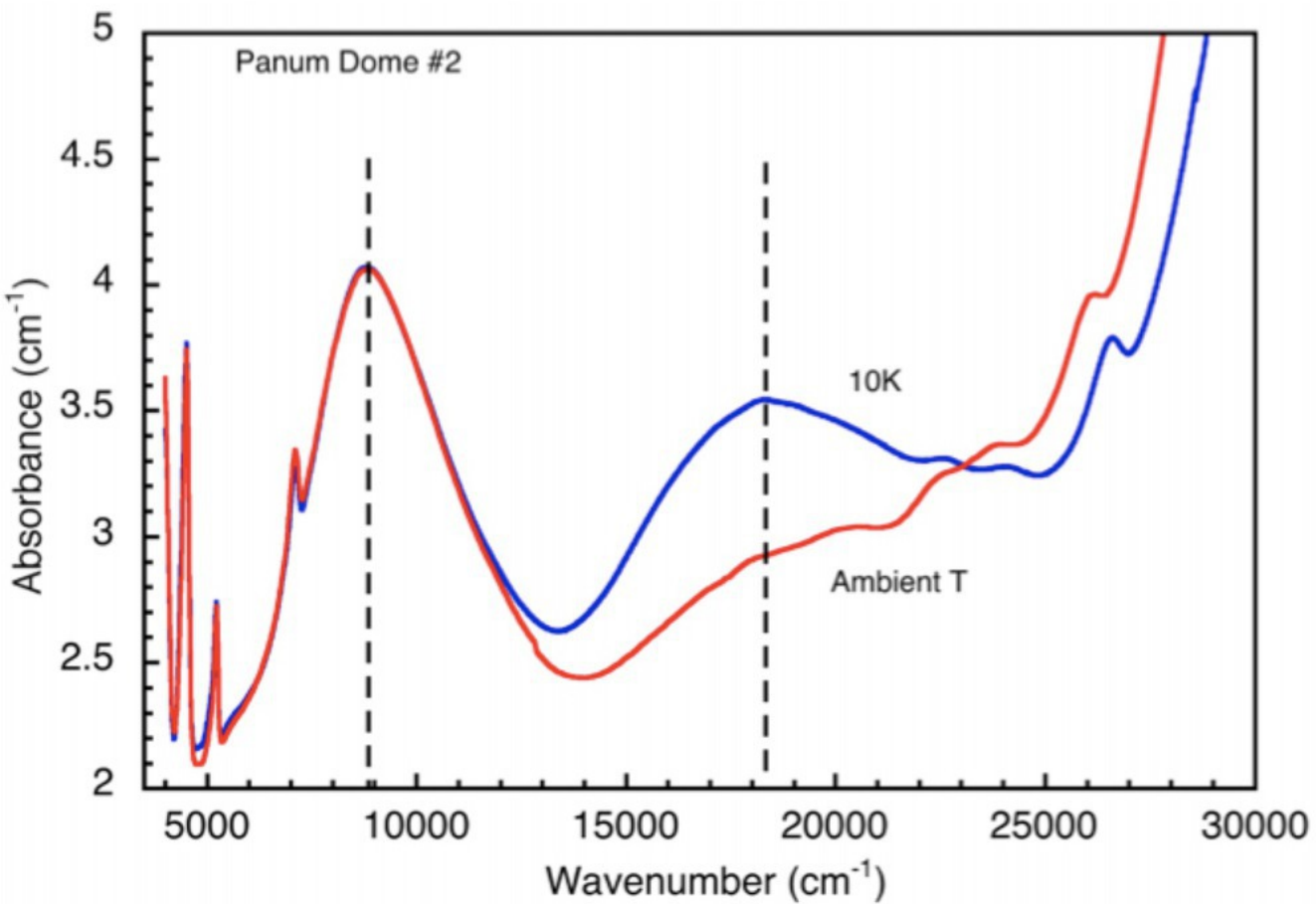
657 S. Si, A. Kotal, T.K. Mandal, S. Giri, H. Nakamura, T. Kohara. Size-controlled synthesis of magnetite  
658 nanoparticles in the presence of polyelectrolytes *Chem. Mater.*, 16 (2004), pp. 3489-3496.

- B. Spiering, F.A. Seifert. Iron in silicate glasses of granitic composition: a Mössbauer spectroscopic study. *Contr. Mineral. Petrol.*, 90 (1985), pp. 63–73.
- R.J. Stevenson, D.B. Dingwell, S.L. Webb, N.S. Bagdassarov. The equivalence of enthalpy and shear stress relaxation in rhyolitic obsidians and quantification of the liquid–glass transition in volcanic processes. *J. Volcanol. Geotherm. Res.*, 68 (1995), pp. 297–306.
- S.J. Stewart, G. Cernicchiaro, R.B. Scorzelli, G. Poupeau, P. Acquafredda, A. De Francesco. Magnetic properties and  $^{57}\text{Fe}$  Mössbauer spectroscopy of Mediterranean prehistoric obsidians for provenance studies *J. Non-Cryst. Solids*, 323 (2003), pp. 188–192.
- S. Taketomi, H. Takahashi, N. Inaba, H. Miyajima. Quantum size effects in light-absorption spectra of magnetite fine particles dispersed in magnetic fluids *J. Phys. Soc. Japan*, 60 (1991), pp. 3426–3432.
- T. Uchino, K. Nakaguchi, Y. Nagachima, T. Kondo. Prediction of optical properties of commercial soda–lime-silicate glasses containing iron. *J. Non-Cryst. Solids*, 261 (2000), pp. 72–78
- V. Vercamer, G. Lelong, H. Hijiya, Y. Kondo, L. Galois, G. Calas. Diluted  $\text{Fe}^{3+}$  in silicate glasses: structural effects of Fe-redox state and matrix composition. An optical absorption and X-band/ Q-band EPR study. *J. Non-Cryst Solids*, 428 (2015), pp. 138–145.
- V. Vercamer, M. O. J. Y. Hunault, G. Lelong, M. W. Haverkort, G. Calas, Y. Arai, H. Hijiya, L. Paulatto, C. Brouder, M. Arrio and A. Juhin. Calculation of optical and  $K$  pre-edge absorption spectra for ferrous iron of distorted sites in oxide crystals. *Phys. Rev. B: Condens. Matter Mater. Phys.*, 94 (2016), p. 245115.
- B. Wang, S. Qu. Discrete dipole approximation simulations of absorption spectra and local electric field distributions of superparamagnetic magnetite nanoparticles. *Laser Phys.*, 23 (2013), p. 045901.
- C. Weigel, L. Cormier, G. Calas, L. Galois, D.T. Bowron. Intermediate-range order in the silicate network glasses  $\text{NaFe}_x\text{Al}_{1-x}\text{Si}_2\text{O}_6$  ( $x = 0, 0.5, 0.8, 1$ ): a neutron diffraction and empirical potential structure refinement modeling investigation *Phys. Rev. B*, 78 (2008), pp. 064202–064212.









EPR derivative (a.u.)

0.2

0.1

0

-0.1

NaCa glass

New Mexico

0

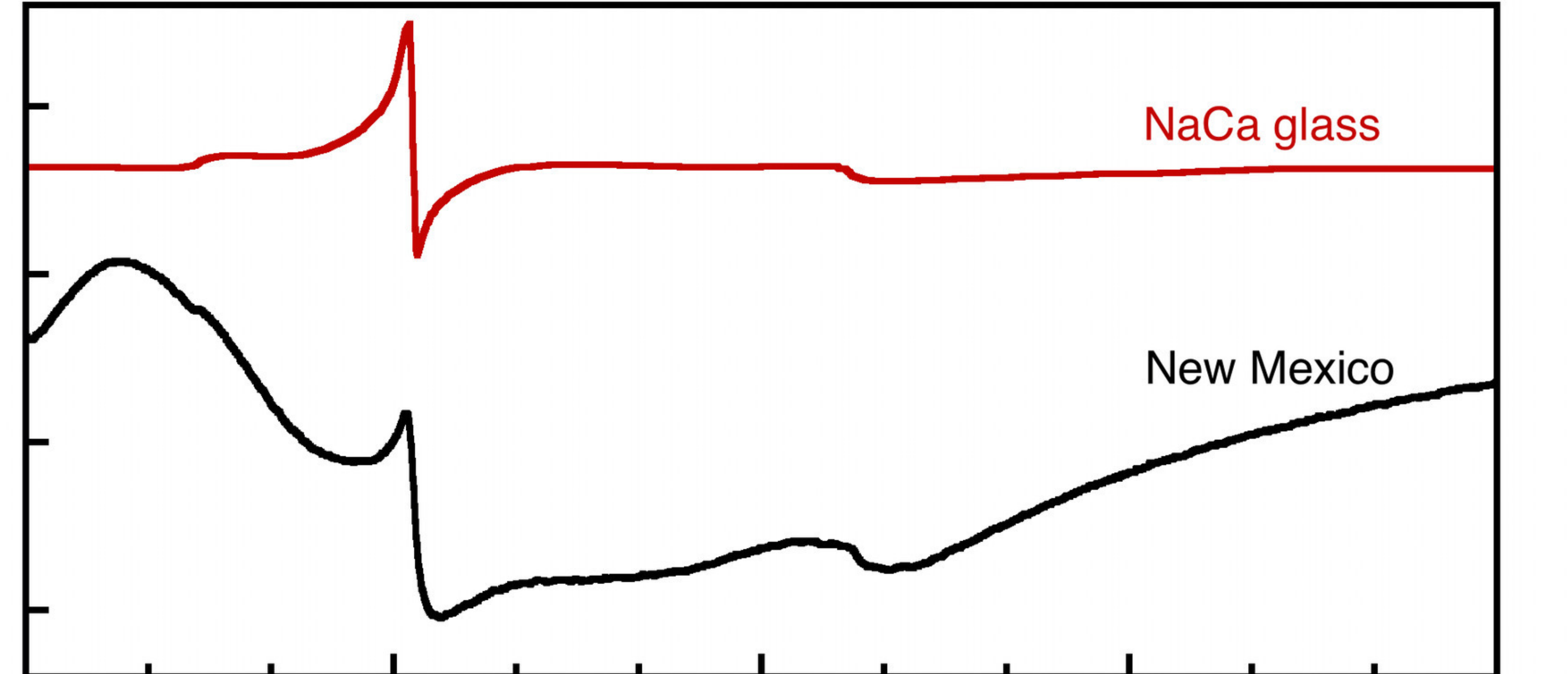
1500

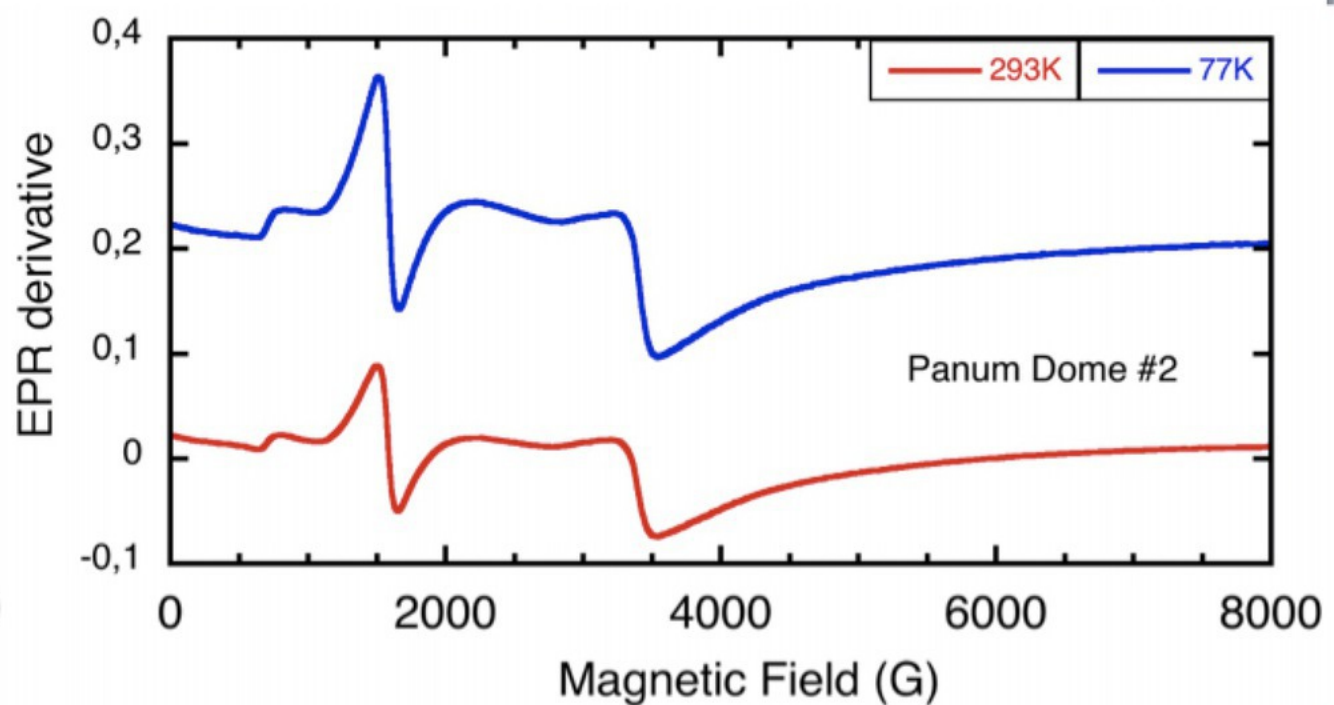
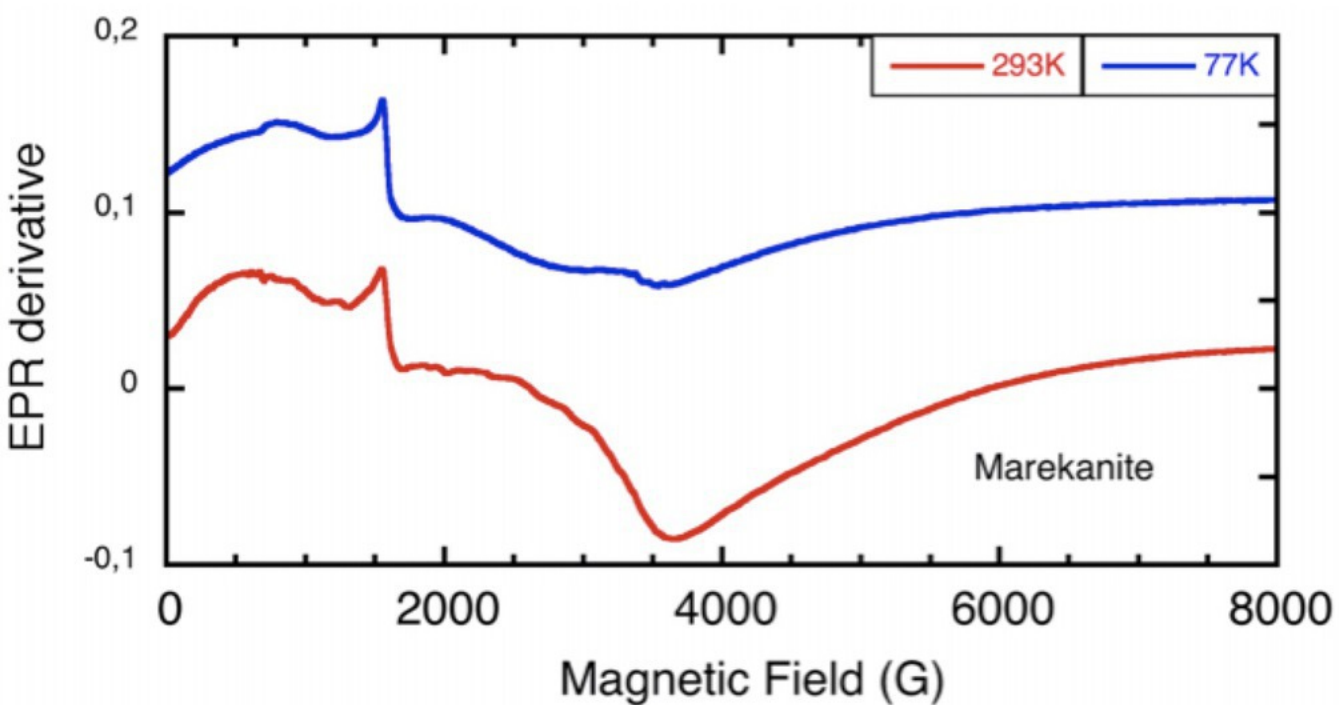
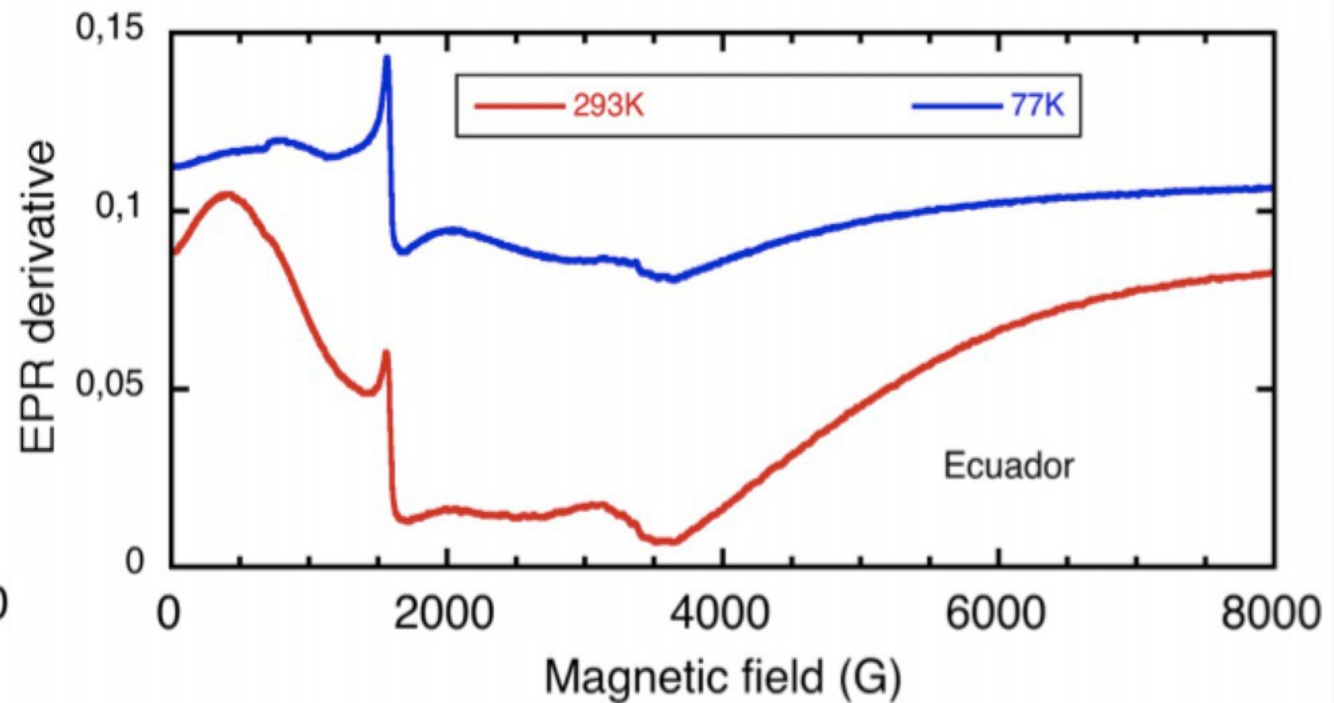
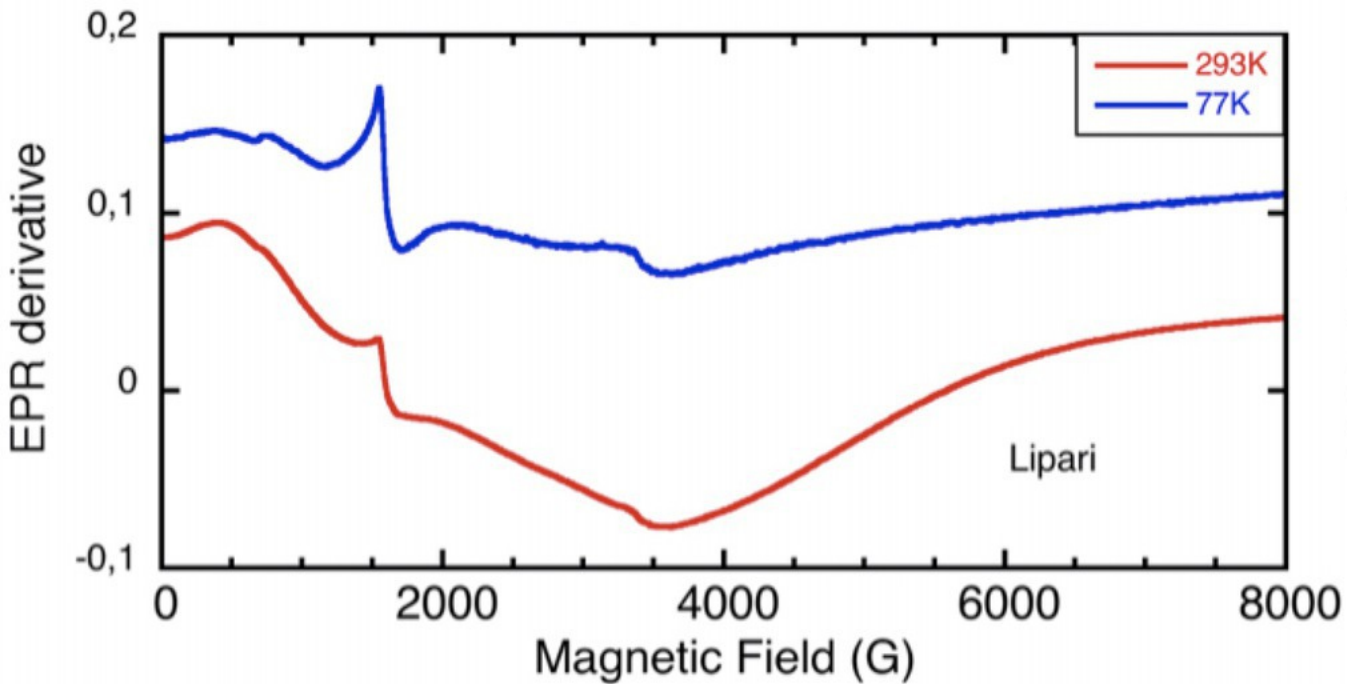
3000

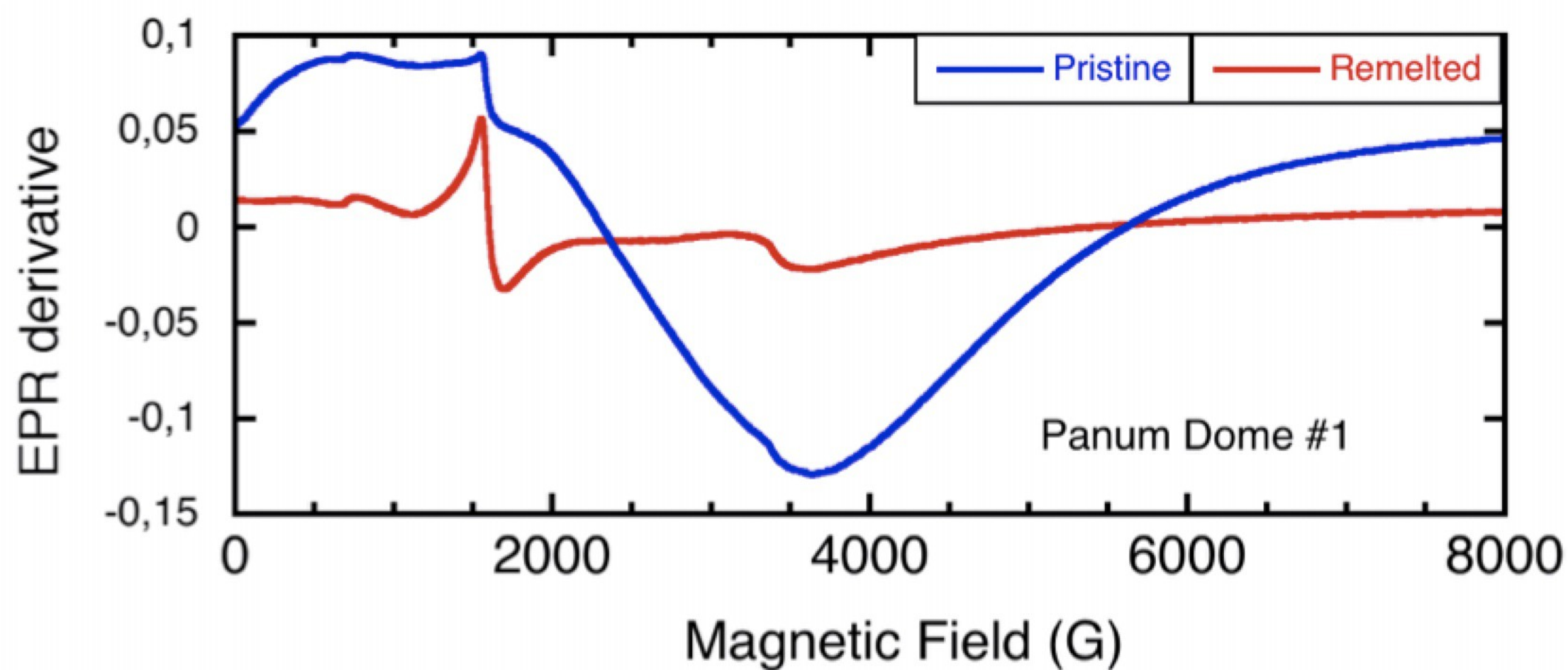
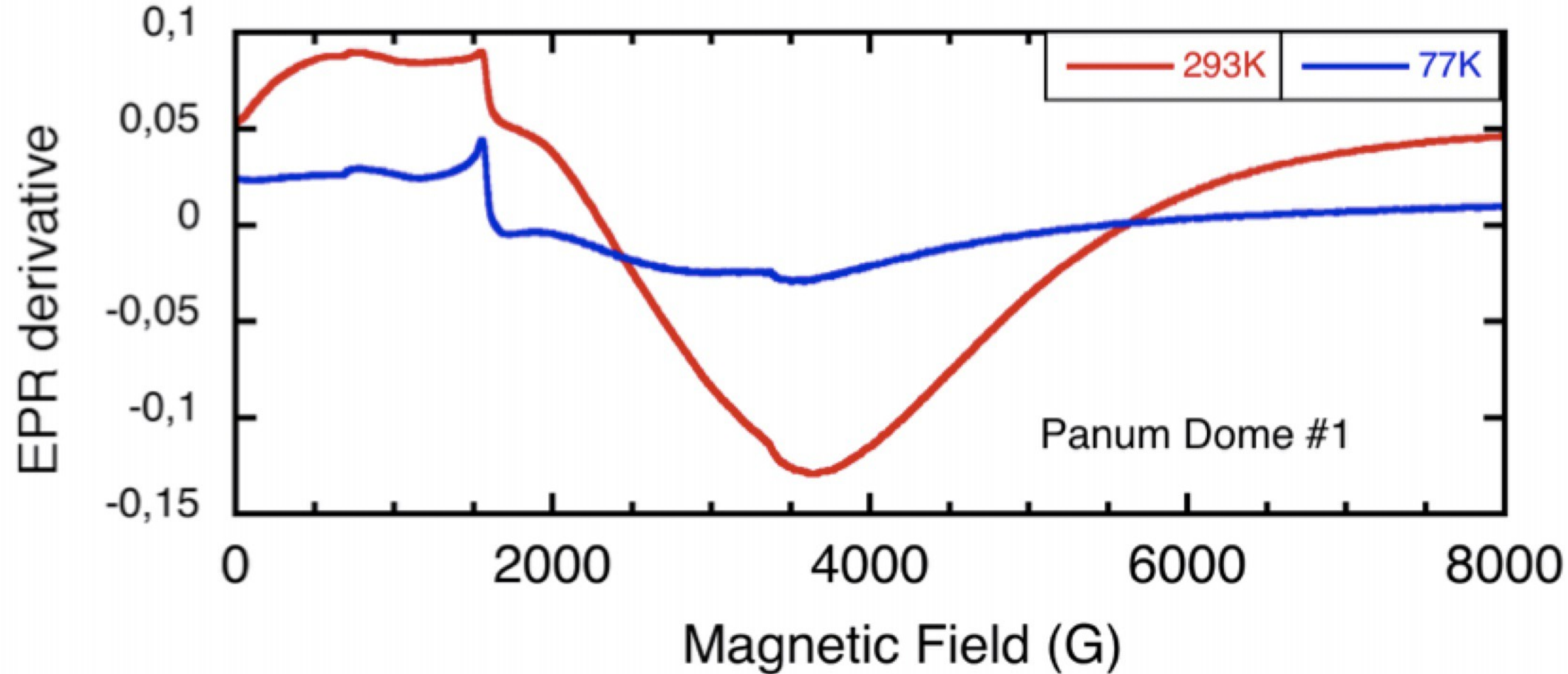
4500

6000

Magnetic field (G)









	≤16+0 wg N=21	16+1–20+0 wg N=36	20+1–24+0 wg N=60	>24 wg N=69	All N=186
Chiari (no/total no (%))	4/13 (30.7%)	33/36 (91.6%)	50/52 (96.1%)	60/61 (98%)	147/162 (90.7%)
Hydrocephalus (no/total no (%))	–	31/36 (86.1%)	46/52 (88.4%)	55/61 (90.1%)	132/149 (88.5%)
Talipes (no/total no (%))	3/21 (14.2%)	13/36 (36.1%)	26/58 (44.8%)	30/69 (43.4%)	72/184 (39.1%)
Upper lesion					
Thoracic (no/total no (%))	5/21 (23.8%)	8/36 (22.2%)	8/60 (13.3%)	8/69 (11.5%)	29/186 (15.6%)
L1 – L2 (no/total no (%))	9/21 (42.8%)	13/36 (36.1%)	16/60 (26.6%)	23/69 (33.3%)	61/186 (32.8%)
L3 – L4 (no/total no (%))	4/21 (19%)	11/36 (30.5%)	25/60 (41.6%)	27/69 (39.1%)	67/186 (36%)
L5 – S1 (no/total no (%))	3/21 (14.2%)	4/36 (11.1%)	11/60 (18.3%)	11/69 (15.9%)	29/186 (15.6%)
N open vertebrae	5 [3-7]	6 [4-8]	5 [4-6]	5 [4-6]	5 [4-7]